

1 **Investigating beach erosion related with tsunami sediment transport at Phra Thong Island,**  
2 **Thailand caused by the 2004 Indian Ocean tsunami**

3  
4 Ryota Masaya<sup>1</sup>, Anawat Suppasri<sup>2</sup>, Kei Yamashita<sup>2</sup>, Fumihiko Imamura<sup>2</sup>, Chris Gouramanis<sup>3</sup>  
5 and Natt Leelawat<sup>4,5</sup>

6  
7 <sup>1</sup>Graduate School of Engineering, Tohoku University, Aoba 6-6-06, Aoba, Sendai 980-0845, Japan

8 <sup>2</sup>International Research Institute of Disaster Science, Tohoku University, 468-1 Aoba, Aramaki-Aza,  
9 Aoba, Sendai 980-0845, Japan

10 <sup>3</sup>Department of Geography, National University of Singapore, 1 Arts Link, Singapore 117570,  
11 Singapore

12 <sup>4</sup>Department of Industrial Engineering, Faculty of Engineering, Chulalongkorn University, Phayathai  
13 Road, Pathumwan, Bangkok 10330, Thailand

14 <sup>5</sup>Disaster and Risk Management Information Systems Research Group, Chulalongkorn University,  
15 Phayathai Road, Pathumwan, Bangkok 10330, Thailand

16 \*Corresponding author.

17 *E-mail address:* ryota.masaya.r6@dc.tohoku.ac.jp (Ryota Masaya)

18  
19 **Abstract**

20 The 2004 Indian Ocean Tsunami and the 2011 Great East Japan earthquake and tsunami caused large-  
21 scale topographic changes in coastal areas. Whereas much research has focused on coastlines that have  
22 or had large human populations, little focus has been paid on coastlines that have little or no  
23 infrastructure. The importance of examining erosional and depositional mechanisms of tsunami events  
24 lies in the rapid reorganisation that coastlines must undertake immediately after an event. A thorough  
25 understanding of the pre-event conditions is paramount to understanding the natural reconstruction of  
26 the coastal environment. This study examines the location of sediment erosion and deposition during  
27 the 2004 Indian Ocean Tsunami event on the relatively pristine Phra Thong Island, Thailand. Coupled  
28 with satellite imagery, we use numerical simulations and sediment transportation models to determine  
29 the locations of significant erosion and the areas where much of that sediment was redeposited during  
30 the tsunami inundation and backwash processes. **Our modelling approach suggests that beaches located**  
31 **in two regions on Phra Thong Island were significantly eroded by the 2004 tsunami**, predominantly  
32 during the backwash phase of the first and largest wave to strike the island. Although 2004 tsunami  
33 deposits are found on the island, we demonstrate that most of the sediment was deposited in the shallow  
34 coastal area, facilitating quick recovery of the beach when normal coastal processes resumed.

35  
36 **1. Introduction**

37 The 2004 Indian Ocean Tsunami and the 2011 Great East Japan earthquake and tsunami caused large-  
38 scale geomorphologic changes in coastal areas during the erosional phases of inflow and outflow (Pari

39 et al., 2008; Goto et al., 2011a; Tanaka et al., 2011; Haraguchi et al., 2012; Hirao et al., 2012; Udo et  
40 al., 2013; Imai et al., 2015). In each tsunami event, the erosional phases translocated sediments onshore  
41 and offshore, and primed the coastal zone for rapid (months to decades) recovery (Choowong et al.,  
42 2009; Ali and Narayama, 2015; Udo et al., 2016; Mieda et al., 2017; Koiwa et al., 2018). However, little  
43 information exists to identify real-time sediment dynamics during the erosional and depositional phases  
44 of tsunami events. In particular, erosive phases mobilize sediments into the onshore (e.g. Jankaew et al.  
45 2008; Gouramanis et al. 2017) and offshore environments (e.g. Feldens et al 2009). Following the  
46 tsunami event, both offshore environment and coastal environments are primed for natural processes to  
47 resume and redistribute sediments onshore to restore the coastal environment to similar pre-tsunami  
48 configurations.

49 However, in many regions, such as the area affected by the 2011 tsunami, extensive engineering  
50 interventions (e.g. levee construction and land level raising) are affecting the natural recovery processes  
51 of the coastal zone. In Japan, many locations have not undergone or been allowed to recover naturally  
52 (Udo et al., 2016; Koiwa et al., 2018), as engineering interventions have taken precedence over natural  
53 recovery processes.

54 Along highly developed and populated coasts that have been affected by tsunami, e.g. Japan, plans  
55 for coastal reconstruction and defenses are typically formulated shortly after a tsunami, preventing  
56 natural recovery processes (Suppasri et al., 2016). These political and engineering interventions make  
57 it difficult to observe or predict the natural recovery processes of coastal areas.

58 Before an understanding of the recovery processes of a tsunami-affected coastal zone can be  
59 achieved, a thorough understanding of the sediment budget must be determined. The relocation of  
60 sediments during the main tsunami erosion and deposition phases establishes the pre-recovery or  
61 baseline conditions upon which natural processes can act to facilitate the recovery of the coastal zone.  
62 To determine the locations of sediment deposition during a tsunami event, the sediment transport  
63 dynamics during the tsunami must be defined.

64 Unfortunately, real-time data from observations has not been possible to establish quantitative  
65 estimates of sediment erosion and deposition during a tsunami event, though qualitative spatial patterns  
66 of sediment process (Udo et al., 2016; Yamashita et al., 2016) have been examined through analyze of  
67 video footage. Prior studies have mainly estimated sediment transport dynamics, such as erosion and  
68 sediment deposition through remote sensing (e.g. Fagherazzi and Du 2008, Choowong et al., 2009;  
69 Liew et al., 2010), and sedimentological and stratigraphic analysis (e.g. Paris et al. 2007; Hawkes et al.  
70 2007; Switzer et al. 2012). However, the information obtained regarding the final results of the sediment  
71 transport process is limited. It is difficult to obtain information on where sediment has eroded and  
72 deposited (e.g. Pham et al., 2018), and whether topographic changes caused by the local sediment runoff  
73 or deposition are the results of action from inflow or backwash (e.g. Choowong et al., 2009; Paris et al  
74 2007; Switzer et al. 2012). This information determines the sediment budget in the system before and  
75 after the tsunami and is therefore important for considering geomorphic recovery.

76 Numerical simulations using wave dynamics of an area can reproduce spatial-temporal variations of

77 the sediment mobility and deposition and can effectively model the sediment transport process using  
78 the wave and sediment characteristics of the natural system. In recent years, the numerical modeling of  
79 tsunami sediment transport has been developed (e.g. Takahashi et al., 2000), improved (e.g. Takahashi  
80 et al., 2011; Apotsos et al., 2011a; Li et al., 2013; Morishita and Takahashi, 2014; Yamashita et al.,  
81 2018) and applied in the field (e.g. Gelfenbaun et al., 2007; Takahashi et al., 2008; Apotsos et al., 2011b;  
82 Apotsos et al., 2011c; Gusman et al., 2012; Li et al., 2014; Arimitsu et al., 2017; Yamashita et al., 2017),  
83 and reproducibility has been confirmed by comparison between the calculated and measured values  
84 (e.g. Li et al., 2012; Ranasinghe et al., 2013; Sugawara et al., 2014a; Yamashita et al., 2015; Yamashita  
85 et al., 2016).

86 An important consideration in the sediment dynamics during catastrophic marine events (e.g. typhoon  
87 and tsunami) is the degree of development and human modification of the coastal zone prior to the  
88 event. Artificial structures, such as sea walls, roads and buildings interfere with washover processes,  
89 and these areas are often targeted from reconstruction and rehabilitation through rapid engineering  
90 reconstruction. Little is known about the recovery processes in sparsely developed and unpopulated  
91 areas. As such, the largely, anthropogenically-undisturbed Phra Thong Island, western Thailand, is an  
92 ideal location to model the sediment dynamics, coastal erosion and deposition following a major  
93 tsunami event.

94 The main objective of this study is to investigate the short-term conditions of sediment transport such  
95 as erosional and depositional process and establishes the baseline sediment conditions that led to further  
96 investigation of the long-term recovery of the Phra Thong Island coastline after the 2004 IOT. We used  
97 tsunami sediment transport calculations to spatio-temporally reproduce the sediment transport  
98 processes occurring during the tsunami and identify zones of sediment deposition in the offshore and  
99 onshore areas and validate these modelling results with published observational data of the 2004 IOT  
100 deposits on the island. Due to the largely natural environment, Phra Thong Island is a rare case that is  
101 useful for verifying tsunami sediment transport models where few artificial features can generate model  
102 uncertainties.

103 Examining the sediment transport processes on Phra Thong Island is also expected to elucidate  
104 phenomena, improve numerical calculation models for the future and is applicable to other areas.  
105 Furthermore, at least three palaeotsunami deposits were identified in areas impacted by the 2004 IOT  
106 on Phra Thong Island (Jankaew et al., 2008; Sawai et al., 2009; Fujino et al., 2009; Fujino et al., 2010;  
107 Prendergast et al. 2012; Brill et al., 2012a, b; Gouramanis et al., 2017; Pham et al., 2018). Thus,  
108 clarifying the sediment transport conditions of the 2004 tsunami will also be important for future  
109 estimations of history, scope and cause of older tsunamis on Phra Thong Island and elsewhere in the  
110 coastal areas of the Indian Ocean.

111

112

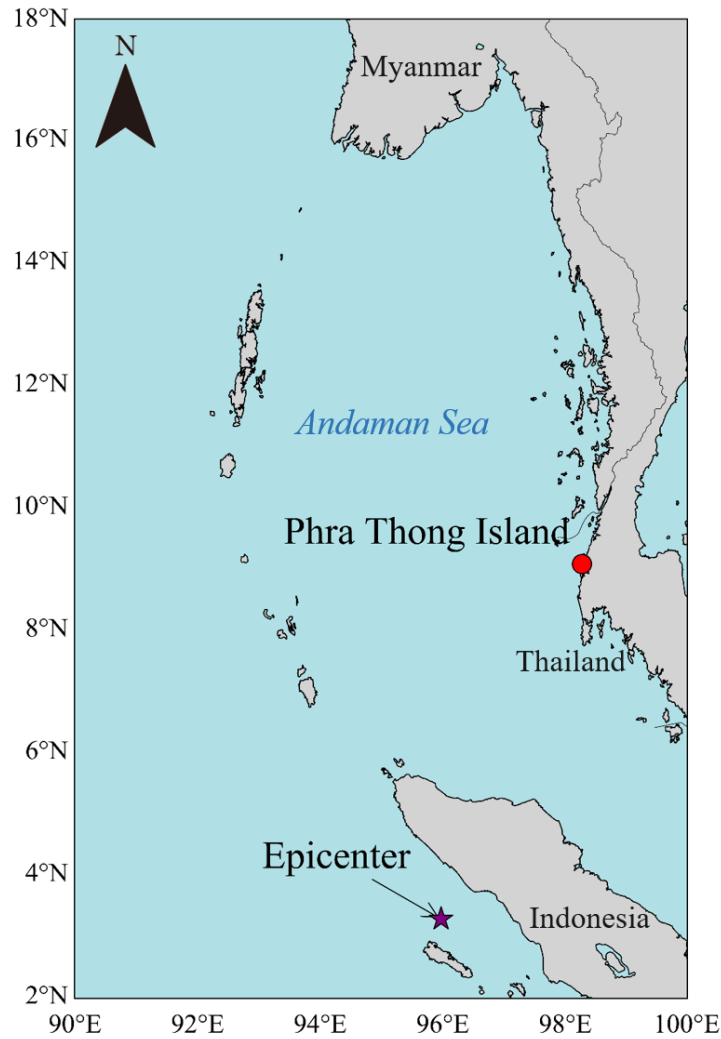


Figure 1 Location of Phra Thong Island

113

114

115

## 116 2. Setting and method

### 117 2.1. Phra Thong Island, Thailand

118 During the 2004 IOT, a wave of approximately 7 m inundated the northern portion of Phra Thong

119 Island (Fig. 1) and measurements up to 20 m were recorded from the southernmost tip of the island

120 (Jankaew et al. 2008). Over 70 people were lost and a village of 100 households disappeared.

121 Geomorphologically, the western coast of the island has a beach ridge sequence trending parallel to the

122 coast, which formed during the sea level regression following mid-Holocene sea level highstand at

123 about 6,000 years ago (Brill et al. 2015). The eastern shore of the island is extensively covered by

124 mangroves along the shores of tidal channels. The island has a tropical climate. Additionally,

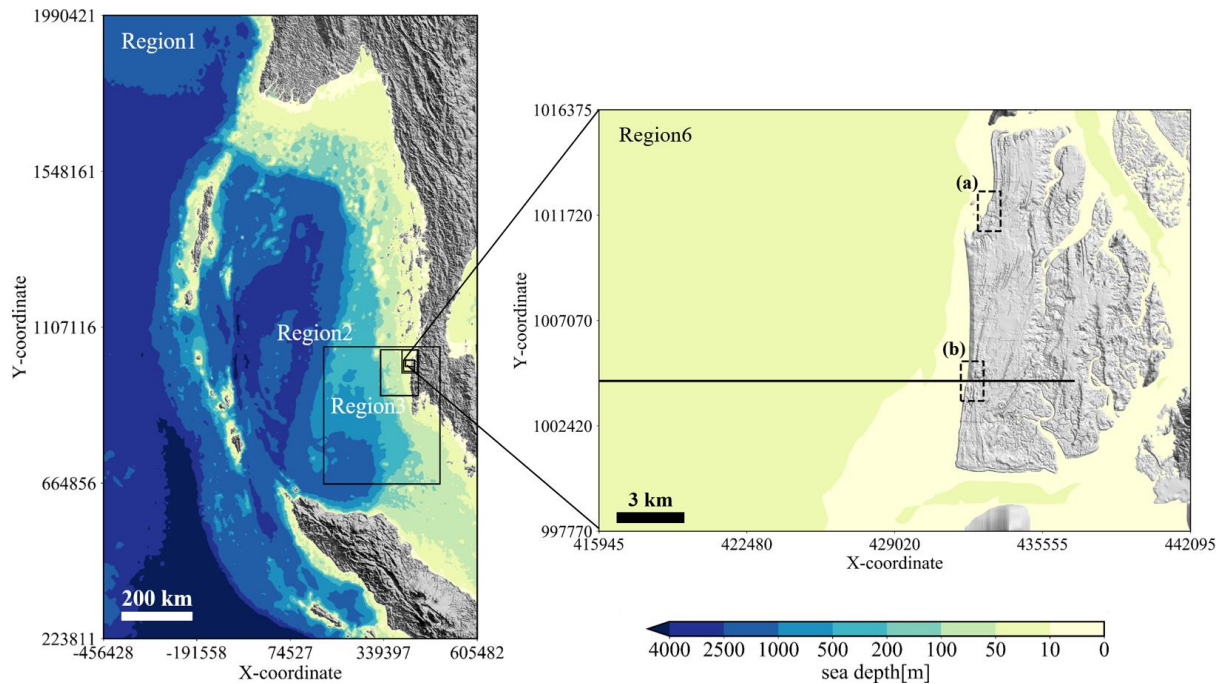
125 palaeotsunami deposits are preserved in swales in the beach ridge system along the western coast of

126 Thailand (e.g. Jankaew et al. 2008; Gouramanis et al. 2017). Furthermore, although local beaches were

127 lost in the 2004 tsunami, satellite photography showed rapid natural recovery within 18 months (e.g.

128 Choowong et al. 2009).

129



130

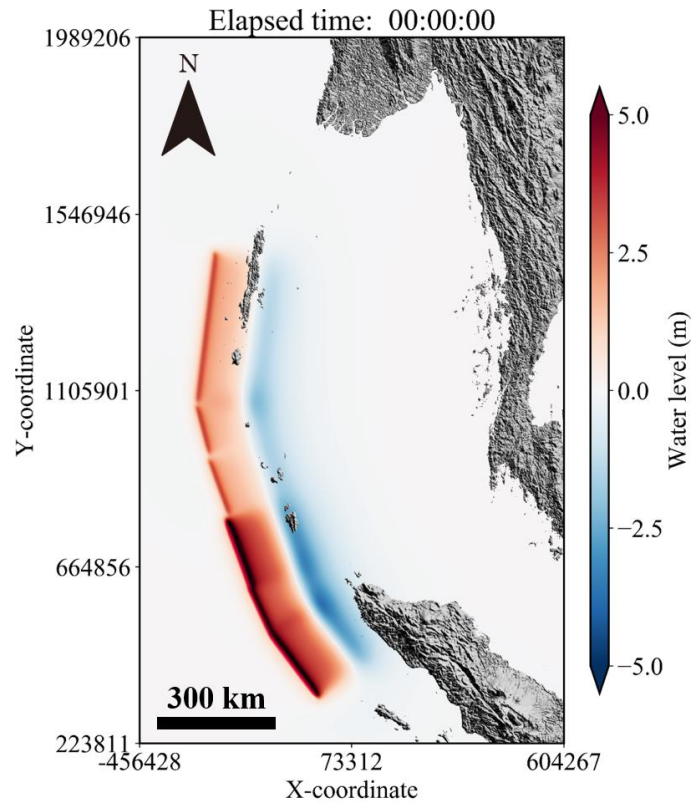
131 Figure 2 Terrain data (The black frame shows Region 1 to Region 6, and the black line in Region 6  
 132 shows the cross-section where calculation was performed. **Dashed squares are the beach where**  
 133 **erosion was confirmed from satellite image.**)

134

135 **2.2. Topography and bathymetry data**

136 The topography and bathymetry data used for the tsunami sediment transport calculations were  
 137 created based on various water depths and elevations. Figure 2 shows the terrain data that were created.  
 138 Topographic data were downsampled from Region 1, which includes the Andaman Sea, to Region 6,  
 139 which includes all of Phra Thong Island. The grid spacing decreases from Region 1 (the spatial grid  
 140 size  $\Delta x_1 = 1,215$  m) to Region 6 ( $\Delta x_6 = 5$  m). In the tsunami sediment transport calculations, UTM zone  
 141 47N was used to geospatially constrain the horizontal modelling coordinates of Phra Thong Island.  
 142 Region 1 is the projection of depth data of the 30-second grid provided by GEBCO (2014) on the  
 143 Cartesian coordinate system UTM 47N. Regions 2–4 use a digital marine chart with 300 m resolution  
 144 based on a survey by the Royal Thai Navy. Regions 5 and 6 use an original 5 m (terrain data) and 15 m  
 145 (sea depth data) grid spacing to create mean terrain and water depth data based on analysis of satellite  
 146 image by EOMAP and elevation data provided by the Land Development Department of Thailand (LDD,  
 147 2018). The terrain data of Region 4, created from the digital marine chart of 300 m resolution, showed  
 148 discontinuity at the boundary with Region 5, which had a higher resolution. The discontinuity was  
 149 therefore removed to the extent possible by interpolation with an inverse distance weighting method  
 150 using all terrain data.

151



152

153

Figure 3 Initial water level after earthquake occurrence

154

155

Table 1 Earthquake fault parameters for calculating initial water level (Suppasri et al., 2011)

Segment No.	1	2	3	4	5	6
Latitude (°N)	3.03	4.48	5.51	7.14	8.47	9.63
Longitude (°E)	94.4	93.3	92.9	92.3	91.9	91.6
Strike (deg)	323	335	340	340	345	7.00
Dip (deg)	15.0	15.0	15.0	15.0	15.0	15.0
Slip (deg)	90.0	90.0	90.0	90.0	90.0	90.0
Length (km)	200	125	180	145	125	380
Width (km)	150	150	150	150	150	150
Dislocation (m)	14.0	12.6	15.1	7.00	7.00	7.00
Depth (km)	10.0	10.0	10.0	10.0	10.0	10.0

156

157

### 2.3. Tsunami source model

158

159

160

161

162

163

The tsunami source model proposed by Suppasri et al. (2011) was used as the tsunami source of the 2004 Indian Ocean Tsunami as the model focused on the coast of Thailand and accurately reproduced the inundation area and surveyed trace height of the 2004 IOT. The fault model is divided into six small faults from satellite image analysis and survey results, and it is assumed that each small fault slides simultaneously and instantaneously. For the tsunami source, the vertical tectonic displacement in each fault was calculated according to Okada (1985). Table 1 shows the fault parameters of each fault and

164 Figure 3 shows the initial water level.

165

## 166 **2.4. Tsunami sediment transport calculation**

### 167 **2.4.1. Tsunami propagation and run-up model**

168 Tohoku University's Numerical Analysis Model for Investigation of Near-field tsunamis, No. 2  
169 (TUNAMI-N2) is based on the nonlinear long wave theory and was used as the tsunami propagation  
170 and run-up model (Imamura, 1996).

$$171 \quad \frac{\partial \eta}{\partial t} + \frac{\partial M}{\partial x} + \frac{\partial N}{\partial y} = 0 \quad (1)$$

172

$$173 \quad \frac{\partial M}{\partial t} + \frac{\partial}{\partial x} \left( \frac{M^2}{D} \right) + \frac{\partial}{\partial y} \left( \frac{MN}{D} \right) + gD \frac{\delta \eta}{\delta x} + \frac{gn^2}{D^{\frac{7}{3}}} M \sqrt{M^2 + N^2} = 0 \quad (2)$$

174

$$175 \quad \frac{\partial N}{\partial t} + \frac{\partial}{\partial x} \left( \frac{MN}{D} \right) + \frac{\partial}{\partial y} \left( \frac{N^2}{D} \right) + gD \frac{\delta \eta}{\delta y} + \frac{gn^2}{D^{\frac{7}{3}}} N \sqrt{M^2 + N^2} = 0 \quad (3)$$

176

177 Here,  $\eta$  is the change in water level from the still-water surface,  $D$  is the total water depth from the  
178 bottom to the water surface, and  $g$  is the acceleration of gravity. The bottom friction is expressed  
179 according to the Manning formula, where  $n$  is Manning's roughness coefficient ( $n = 0.025$ ).  $M$  and  $N$   
180 are the total flow fluxes in the  $x$  and  $y$  directions, respectively, and are given by integrating the horizontal  
181 flow velocity  $u, v$  from the water bottom  $h$  to the water surface  $\eta$ . It is assumed that the horizontal flow  
182 velocity is uniformly distributed in the vertical direction.

183 The nonlinear long wave theory consists of a continuous equation that is derived from (1) the  
184 principle of conservation of mass (continuity equation) and (2) the conservation of momentum  
185 (equation of motion). These two equations are obtained by vertically integration from the seabed to the  
186 water surface.

187 When the water depth is about 50 m or less, the effects of the 2nd, 3rd and 5th terms of the advection  
188 and seabed friction terms (Equations 2 and 3) are reduced, therefore wave theory that omit these terms  
189 is often used at depths shallower than 50 m. Meanwhile, the Message Passing Interface (MPI) parallel  
190 was implemented in the model for highly efficient calculations. Both the advection term and the bottom  
191 friction term were therefore considered in the calculations without reducing accuracy in deeper waters.

192 **The reproducibility of the calculated results is based on the tsunami height data (IUGG; available at**  
193 **<http://www.nda.ac.jp/~fujima/TMD/index.html>) for the 2004 IOT and is discussed using the geometric**  
194 **mean  $K$  and geometric standard deviation  $\kappa$  proposed by Aida (1978).**

195

196 
$$\log K = \frac{1}{n} \sum_{i=1}^n \log K_i \quad (4)$$

197

198 
$$\log \kappa = \sqrt{\frac{1}{n} \left\{ \sum_{i=1}^n (\log K_i)^2 - n(\log K)^2 \right\}} \quad (5)$$

199

200 Here,  $n$  is the number of points,  $R_i$  is the tsunami height at the  $i^{\text{th}}$  point,  $H_i$  is the calculated value at the

201  $i^{\text{th}}$  point, and  $K_i = R_i/H_i$ .

202

203 **2.4.2. Sediment transport model**

204 For the tsunami movable bed model, we used the numerical Sediment Transport Model (STM)

205 proposed by Takahashi et al. (2000), which solves the time evolution of sediment transport considering

206 the exchange sediment volume of the bed and suspended load layers according to the flow conditions

207 of the nonlinear long wave theory-based TUNAMI-N2 model. For each time step in the finest

208 calculation region (region 6), the STM receives the total flow fluxes from TUNAMI-N2 and calculates

209 the change of seafloor and land surface and feeds this to the next time step of the TUNAMI-N2 model.

210 This model divides tsunami sediment transport into a bed load layer, where sediment grains pull, and

211 a suspended load layer, where sediment grains float. The governing equations consist of continuous

212 equations for the bed load layer and the suspended load layer:

213

214 
$$\frac{\partial Z_B}{\partial t} + \frac{1}{1 - \lambda} \left( \frac{\partial q_{B,x}}{\partial x} + \frac{\partial q_{B,y}}{\partial y} + w_{\text{ex}} \right) = 0 \quad (6)$$

215

216 
$$\frac{\partial Ch_S}{\partial t} + \frac{\partial CM}{\partial x} + \frac{\partial CN}{\partial y} - w_{\text{ex}} = 0 \quad (7)$$

217

218 Here,  $\lambda$  is the sediment grain porosity,  $Z_B$  is the bottom height from the reference plane,  $q_B$  is the amount

219 of bed load sediment,  $C$  is the average suspended load layer concentration,  $h_s$  is the suspended load

220 layer thickness (= total water depth), and  $M, N$  are the water discharges in the  $x$  direction and  $y$  direction,

221  $w_0$  is the sedimentation velocity of the sediment grains.

222 Equation (6) is a continuous equation for within the bed load layer. The first term is the exchange

223 sediment volume with the bottom, the second term is the balance of sediment flow volume moving in

224 a tractive form in the flow direction, and the third term defines the balance of suspension flux, caused

225 by diffusion, and sedimentation flux, caused by gravity, as the exchange sediment volume between the

226 bed load layer and the suspended load layer.

227 Equation (7) is a continuous equation for within the suspended load layer. The first and second terms

228 are bed load sediment moving in a suspended state in the flow direction, the third term is the exchange



229 sediment volume between the bed load layer and the suspended load layer, and the fourth term is the  
 230 increase or decrease of the sediment flow in the suspended load layer.

231 In Equations (8) and (9), the equations defining the bed load sediment volume  $q_B$  and the equation  
 232 defining the exchange sediment volume  $w_{ex}$  of the bed load layer and suspended load layer are  
 233 necessary, but according to Takahashi et al. (2000), they are obtained by the following:

$$235 \quad q_{B,x,y} = \alpha \sqrt{sgd^3} (\tau_* - \tau_c)^{\frac{3}{2}} \quad (8)$$

$$236 \quad w_{ex} = \beta \sqrt{sgd} (\tau_* - \tau_c)^2 - w_0 C \quad (9)$$

$$237 \quad \tau_* = \frac{u_*^2}{sgd} \quad (10)$$

240 Here,  $\alpha$  is the coefficient of the bed load sediment volume equation,  $\beta$  is the coefficient of the suspension  
 241 volume equation,  $s$  is the submerged density of the sand particles ( $s = \rho_s/\rho_w - 1$ ;  $\rho_s$  and  $\rho_w$  are the  
 242 density of sand particles and water, respectively;  $\rho_s = 2.65 \text{ g/cm}^3$  and  $\rho_w = 1.0 \text{ g/cm}^3$ ),  $g$  is the  
 243 acceleration of gravity,  $d$  is grain diameter,  $w_0$  is the sedimentation velocity of the sediment grains,  $\tau_*$  is  
 244 the Shields number (Equation (10)),  $\tau_c$  is the limit Shields number,  $u_*$  is the friction velocity obtained  
 245 from the Manning formula ( $u_*^2 = gn_s^2 M |M| / D^{7/3}$ ).  $n_s$  is the roughness coefficient for STM. Note that  
 246 the value of the roughness coefficient  $n$  used the tsunami calculation differs from  $n_s$ .

247 The grain-size dependent parameter for bed load ( $\alpha$ ) and exchange rate ( $\beta$ ) in Equation (8) and (9)  
 248 are derived from Equations (11) and (12) based on the hydraulic experiments by Takahashi et al. (2011):

$$249 \quad \alpha = 9.8044e^{-3.366d} \quad (11)$$

$$250 \quad \beta = 0.0002e^{-6.5362d} \quad (12)$$

251 However, the functions should not be applied when  $d$  is outside the 0.166 mm to 0.394 mm range as he  
 252 validity of extrapolated  $d$  values may produce erroneous results.

$$253 \quad w_0 = \sqrt{sgd} \left( \sqrt{\frac{2}{3} + \frac{36v^2}{sgd^3}} - \sqrt{\frac{36v^2}{sgd^3}} \right) \quad (13)$$

254 Equation (13) is a settling velocity of the sand particles by Rubey (1933). Here,  $v$  is the kinematic  
 255 viscosity coefficient ( $v = 0.0139 \text{ cm}^2/\text{s}$ ).

256 Considering the effect from the bed slope (Watanabe et al., 1984), the formulation of the bed load,  
 257  $q_B$ , Equation (6), is rewritten as  $Q_B$  as shown in Equations (14) and (15):

263

$$264 \quad Q_{B,x} = q_{B,x} - |q_{B,x}| \varepsilon \frac{\partial Z_B}{\partial x} \quad (14)$$

265

$$266 \quad Q_{B,y} = q_{B,y} - |q_{B,y}| \varepsilon \frac{\partial Z_B}{\partial y} \quad (15)$$

267

268 where  $\varepsilon$  is a diffusion coefficient of the sediments ( $\varepsilon = 2.5$ ; Sugawara et al., 2014a).

269

270

271

272

273

274

275

Sediment transport during tsunami largely occurs as suspension (Takahashi et al., 2000). In such situations, suspended sediments are maintained in the water column by turbulence while the energy of the turbulence is dissipated due to the increased suspended sediment concentration. This induced an equilibrium state in which no further sediment supply from the bottom occurs. The resulting concentration is called the saturated sediment concentration. The expression for saturation concentration of suspended sediments  $C_s$  is applied as (Van Rijn, 2007; Sugawara et al., 2014a):

$$276 \quad C_s = \frac{\rho_w}{\rho_s - \rho_w} \frac{e_s n_s^2 u^3}{h_s^{4/3} w_0 - e_s n_s^2 u^3} \quad (16)$$

277

278

279

280

281

282

283

284

where  $e_s$  is the efficiency coefficient ( $e_s = 0.025$ ; Bagnold, 1966). Note that in the sediment transport calculation, the saturation concentration of suspend sediments given by Equation (16) is applied entrainment of sediment from the bottom layer. Namely, sediment supply from the bottom to the water column (suspended load layer) by  $w_{ex}$  is not permitted if  $C \geq C_s$ . However, supersaturation ( $C \geq C_s$ ) due to sediment advection, or sudden decrease of  $C_s$  due to the change of flow parameters, is permitted. In this calculation, when  $C$  exceeds maximum concentration  $C_{max}$  was set to 0.377, based on the observed value (Xu, 1999a, 1999b).

285

286

287

288

289

290

In Equation (6) and Equation (7), the bottom height ( $Z_B$ ) is determined from the reference plane, and the average suspended sediment concentration ( $C$ ) are the initial values before the tsunami and the flow flux ( $M$ ). Because suspended sediment thickness ( $h_s$ ) is given by the equation of motion of a fluid and the continuous equation, sea level fluctuation can be determined over time. Further, the MPI parallel was implemented to enable relatively efficient wide area calculations (e.g. Yamashita et al. 2016).

## 291 **2.5. Calculation conditions**

292

293

294

295

The initial conditions for the numerical simulations used the terrain data (Figure 2) and tsunami source (Figure 3). The simulations were performed using a 3:1 nested grid that increased the resolution a 1215 m<sup>2</sup> grid to a 5 m<sup>2</sup> grid. Additionally, the target region of the sediment transport calculation was limited to Region 6, with a grid spacing of 5 m<sup>2</sup>.

296

297

The simulations were calculated over a 0.05 second increment with a 6-hour period in which the test case with a 12 hour period showed the suspended sediment concentration in the vicinity of the shoreline

298

Table 2 Set parameters for sediment transport calculations

Parameter	Value
Coefficient of bed load sediment volume equation $\alpha$	6.40
Coefficient of suspension sediment volume equation $\beta$	$8.70 \times 10^{-5}$
Critical friction $u_c$	0.0137 m/s
Sedimentation velocity of sediment grains $w_0$	0.00971 m/s

299

300 decreased and stabilized. Therefore, 6-hour simulation was used for the reproduction of the 2004  
301 tsunami as well as further sensitivity analysis of the grain size and roughness coefficient.

302 For the bottom conditions of STM, the roughness coefficient was fixed at  $n_s = 0.030 \text{ s/m}^{1/3}$ , and the  
303 entire area of Region 6 was considered the movable bed. In general, when simulating tsunami sediment  
304 transport, it is necessary to determine the roughness coefficient according to land use. However, since  
305 there is no land use map before the tsunami on Phra Thong Island, a fixed value was used, similar to  
306 previous studies (e.g. Sugawara et al., 2014a, b; Yamashita et al., 2015; Yamashita et al., 2016). However,  
307 Sugawara et al. (2014a) showed that the variation in Manning's roughness coefficient for the sand beds  
308 may affect the general distribution pattern of sediment deposits and erosions across the artificial  
309 topographic features with much higher roughness coefficient such as artificial canals, roads and  
310 populated residential areas. Therefore, a sensitivity analysis on the roughness coefficient was performed.  
311 Phra Thong Island has no such artificial topographic features and using the single roughness coefficient  
312 should sufficiently capture the overall roughness. However, to ensure robust conclusions, a sensitivity  
313 analysis for two bottom conditions was performed at  $n_s = 0.025 \text{ s/m}^{1/3}$  and  $n_s = 0.035 \text{ s/m}^{1/3}$ , which are  
314 within the range of previously used estimates of roughness (e.g. Sugawara et al., 2014a, b).

315 The grain size was based on one sediment data set (Gouramanis et al., 2017) from the locally eroded  
316 region, and was considered as a representative value for all of the tsunami sediment grain sizes. A  
317 uniform grain size of  $d = 0.127 \text{ mm}$  was used. The critical Shields number  $\tau_c$  in Equations (9) and (10)  
318 was obtained using Equations (17) and (18) according to Iwagaki et al. (1956):

319

$$320 \quad \tau_c = u_c^2 \rho \quad (17)$$

321

$$322 \quad u_c^2 = 8.41 d^{\frac{11}{32}} \quad (18)$$

323

324 Here,  $u_c$  is the critical friction and  $\rho$  is the density of water. Table 2 shows each parameter used for the  
325 sediment transport calculations in this study.

326 The numerical model used in this paper can only consider a single grain size, so the model cannot  
327 resolve the grading observed in the sand layers (e.g. Gouramanis et al., 2017). Additionally, initial bed  
328 grain size can have a large effect on erosion and deposition (e.g. Apotsos et al., 2011b; Sugawara et al.,  
329 2014a; Jaffe et al., 2016). Furthermore, the sediment data we used to set the grain size is from a single

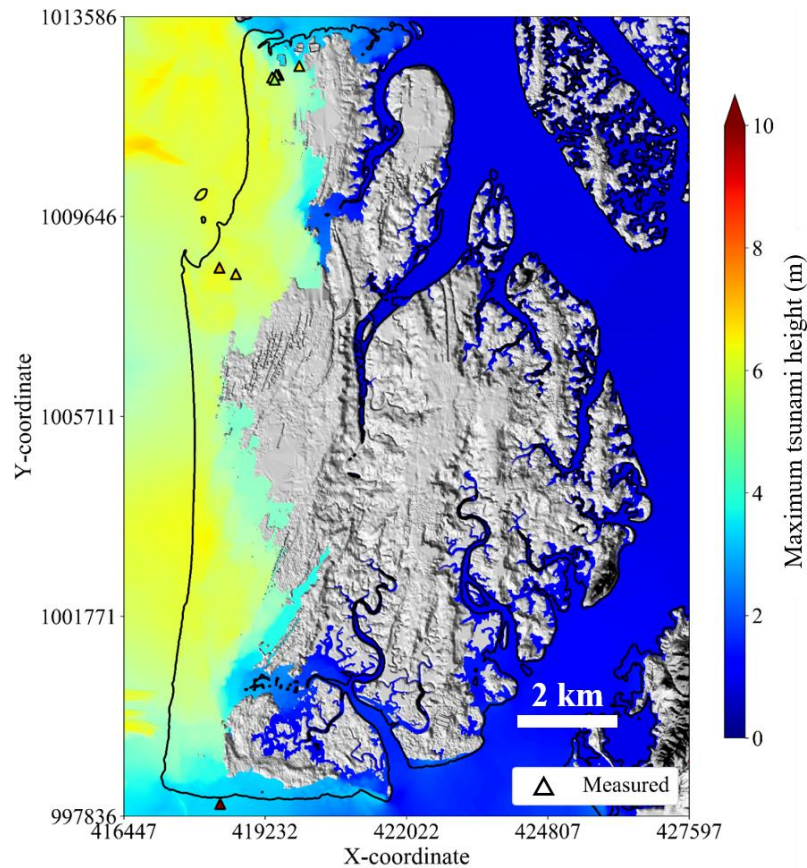


Figure 4 Comparison of calculated and measured maximum tsunami height

330  
331  
332

333 location in the north of the island, and is assumed to be a representative grain size for the tsunami  
334 deposits. As such we performed a sensitivity analysis on the grain size. Pham et al. (2018) investigated  
335 the surface grain size of the offshore (water depth > 15 m), nearshore (water depth < 15 m), and onshore  
336 on Phra Thong Island, which they considered to be the source of sediments that formed the tsunami  
337 deposits. Pham et al. (2018) recorded a mean grain size of 0.314 mm in the offshore area, 0.129 mm in  
338 the nearshore area, and 0.285 mm in the onshore area. Based on these mean grain sizes, we conducted  
339 a sensitivity analysis for two grain sizes (0.285 mm and 0.314 mm representing the offshore and onshore  
340 sediments)

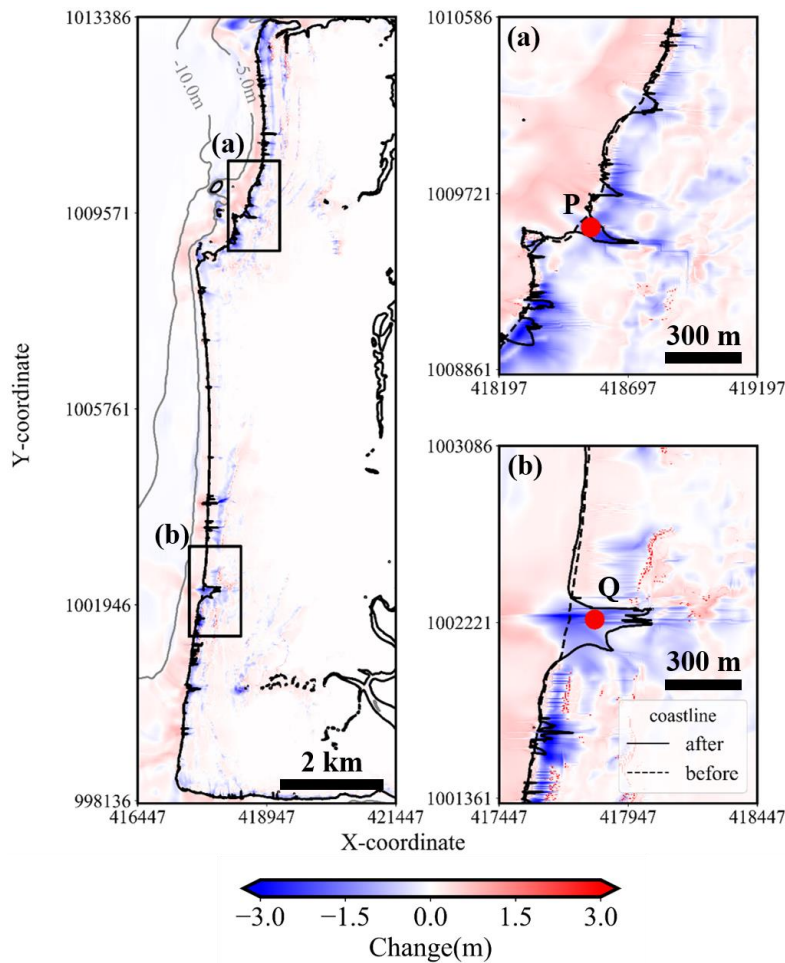
341

### 343 3. Results

#### 344 3.1. Verification of reproducibility

##### 345 3.1.1. Tsunami height

346 Figure 4 shows the results of the calculation of the maximum tsunami heights and the seven measured  
347 tsunami heights on Phra Thong Island. From Equations (4) and (5),  $K = 1.16$  and  $\kappa = 1.4$  are obtained.  
348 The Japan Society of Civil Engineers (2012) consider  $0.95 < K < 1.05$  and  $\kappa < 1.45$  as guides for  
349 evaluating reproducibility of tsunami numerical calculations. Although the  $K$  value is slightly higher  
350 than the guideline but this is because of an uncertain 19.6 m measured in the southern part of the Island.  
351 Additionally, the source model used in this calculation gives  $K = 0.84$  and  $\kappa = 1.3$  for reproducibility of



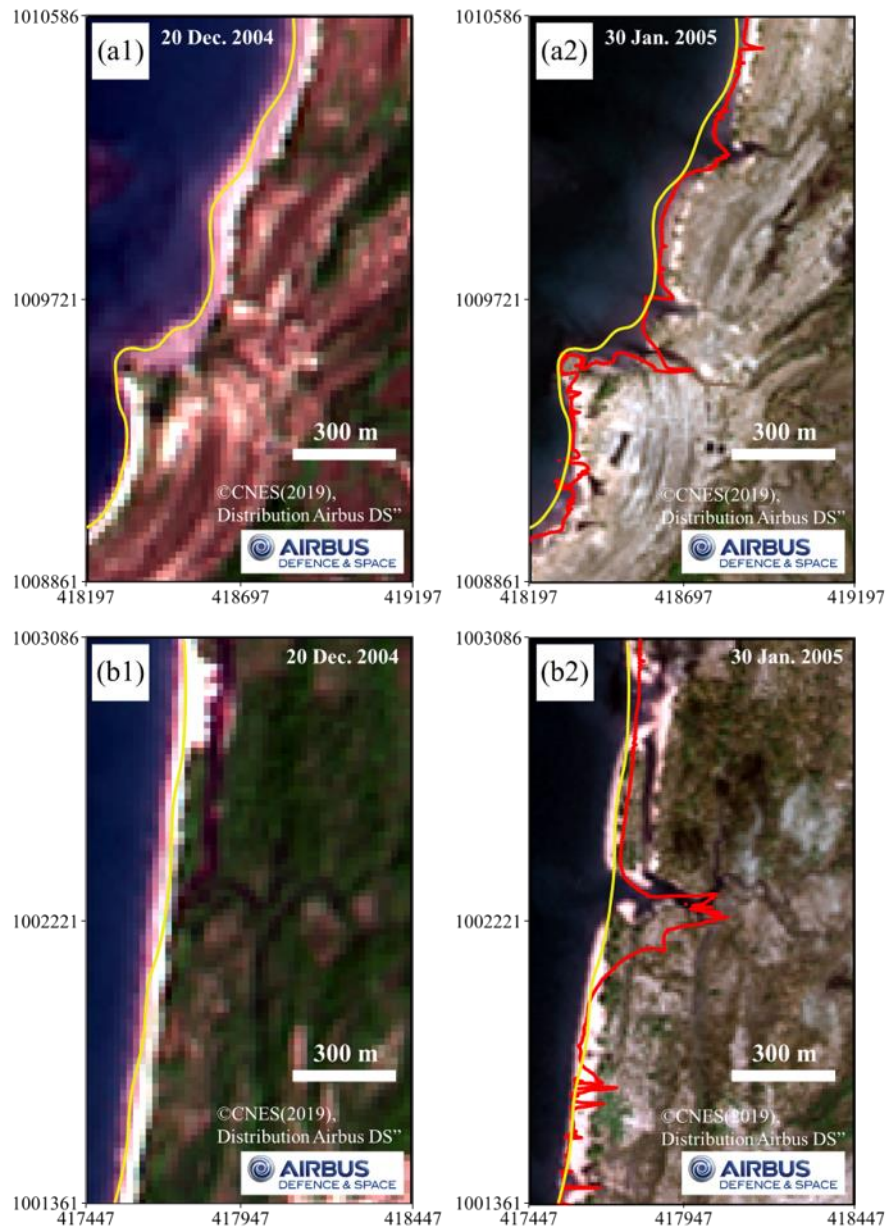
352

353 Figure 5 Topographic change and shoreline position caused by the tsunami (solid & dashed lines show  
 354 that the coastline after and before the tsunami in the simulation, P and Q are the points confirmed  
 355 local beach erosion in region (a) and (b), blue and red mapping show erosion and deposition after the  
 356 tsunami in the simulation)  
 357

358 tsunami height in the wide area along the coast of Thailand (Suppasri et al., 2011). Therefore, it can be  
 359 said that this calculation has the same tsunami reproducibility as the previous study.  
 360

### 361 3.1.2. Shoreline changes

362 Our sediment transport models identify the locations of significant sediment erosion, which are  
 363 confirmed from post-tsunami satellite images. Figure 5 shows the pre-2004 IOT topographical and  
 364 geomorphological features (dashed line) and the modelled changes caused by the tsunami (solid line).  
 365 Erosion typically occurs locally where small tidal channels breach the youngest beach ridge system  
 366 (Figure 5(a) and 5(b)). Comparison with the satellite image shows that the position of erosion in both  
 367 regions is consistent (Figure 6). Although the actual amount of erosion is unknown, this indicates that  
 368 the planar spread of the eroded component can be well reproduced by the calculation. Region (a) was  
 369 further investigated in detail, as the area corresponds to the point where sediment outflow occurred  
 370 (Jankaew et al., 2008).



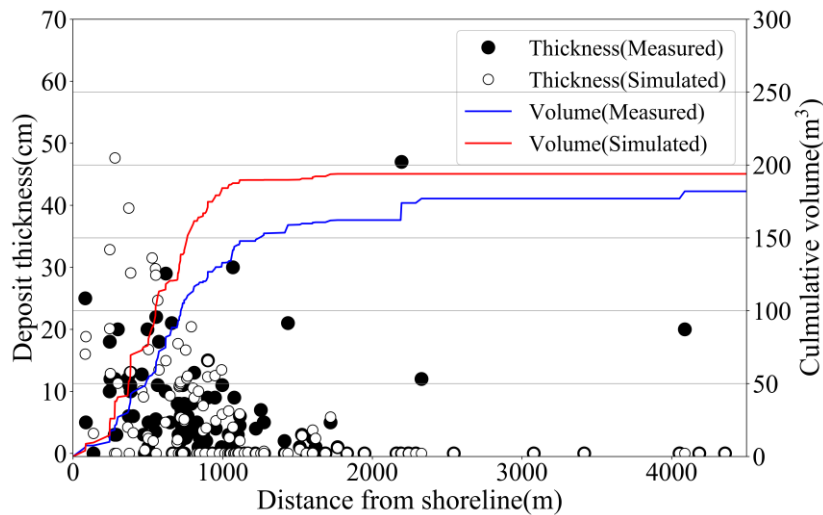
371  
372  
373  
374  
375  
376  
377  
378  
379  
380

Figure 6 Comparison of observed shoreline position from Figure 5 region (a) and (b) derived from satellite images before and after the tsunami (20 Dec. 2004 and 30 Jan. 2005), which is overlain by the modelled extent of erosion showing that the modelled results closely match the observed changes. The red line is the calculated shoreline after the tsunami, and the yellow line is the shoreline before the tsunami (© CNES, 2019, Distribution Airbus DS”).

a1) Satellite image before the tsunami in region (a), a2) Satellite image after the tsunami in region (a),  
b1) Satellite image before the tsunami in region (b), b2) Satellite image after the tsunami in region (b)

### 3.1.3. 2004 IOT onshore sediment deposition

In addition to the erosional features, the model simulated the deposition of 2004 IOT sediments across the island. The thickness of these simulated deposits are compared with 133 measured 2004 IOT deposit



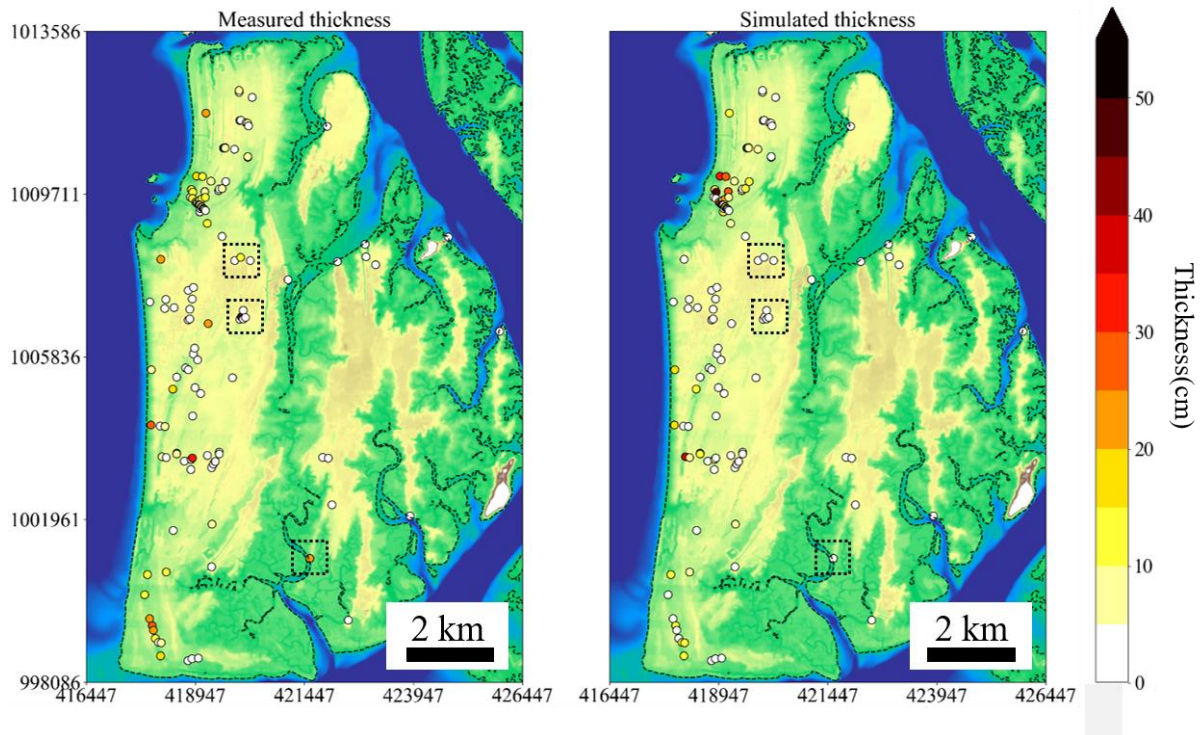
384  
385  
386  
387  
388  
389

Figure 7 Comparison of field measured and simulated tsunami deposit thickness using a representative grain size of  $d = 0.127$  mm. Black point shows the measured thickness by Jankaew et al. (2008) and Gouramanis et al. (2017), white point shows the simulated thickness. Blue and red line show the cumulative curves of measured data and simulated data.

390 thicknesses (Jankaew et al., 2008; Gouramanis et al., 2017). Figure 7 shows a comparison of layer  
391 thicknesses at each site (black circles for measured results and white circles for simulated results), which  
392 shows that most of the sites are overestimated within 1 km from the shoreline and underestimated at  
393 distances greater than 2 km from the shoreline. The model specification and topographical data can be  
394 considered as the major causes of this error.

395 First, considering the overestimation within 1 km of the inundation distance, it is found that the STM  
396 has a setting of the maximum suspended concentration,  $C_{max}$  as 37.7% (Xu, 1999a and 1999b). The  
397 computed suspended concentration in this area is higher than  $C_{max}$ . Therefore, the surplus sediment is  
398 forced to be deposited in this zone causing overestimation. Pham et al. (2018) found that the source of  
399 tsunami deposits in Phra Thong Island is mainly the sediment from the nearshore zone. In other words,  
400 the first wave, which had the highest wave height, eroded a large amount of sediment in the nearshore  
401 and transported a large amount of sediment inland. Therefore, it is considered that the maximum  
402 concentration was reached during the first wave run-up because of the very high concentration of  
403 suspended sediment, which led to the overestimation of the forced sedimentation in the simulation.

404 Second, considering the underestimation of the deposition in inundation distances of 2 km or more,  
405 the most likely reason is the computational grid and the model specification. Previous studies have  
406 shown that tsunami deposits are highly affected by locality features (e.g. Sugawara et al., 2014a;  
407 Watanabe et al., 2018). As shown in three locations with the actual measured deposit thickness (dashed  
408 boxes) in Fig. 8, it can be seen that most of the measured thickness is zero which indicate and support  
409 the reasons of localized deposition. Although the computational grid is very fine ( $\Delta x_6 = 5$  m), it is  
410 difficult to reproduce local sedimentation with averaged elevation data. In addition, this STM uses only  
411 a single grain size and can only model deposits consisting of sand grain-sizes. Sugawara et al. (2014a)



412

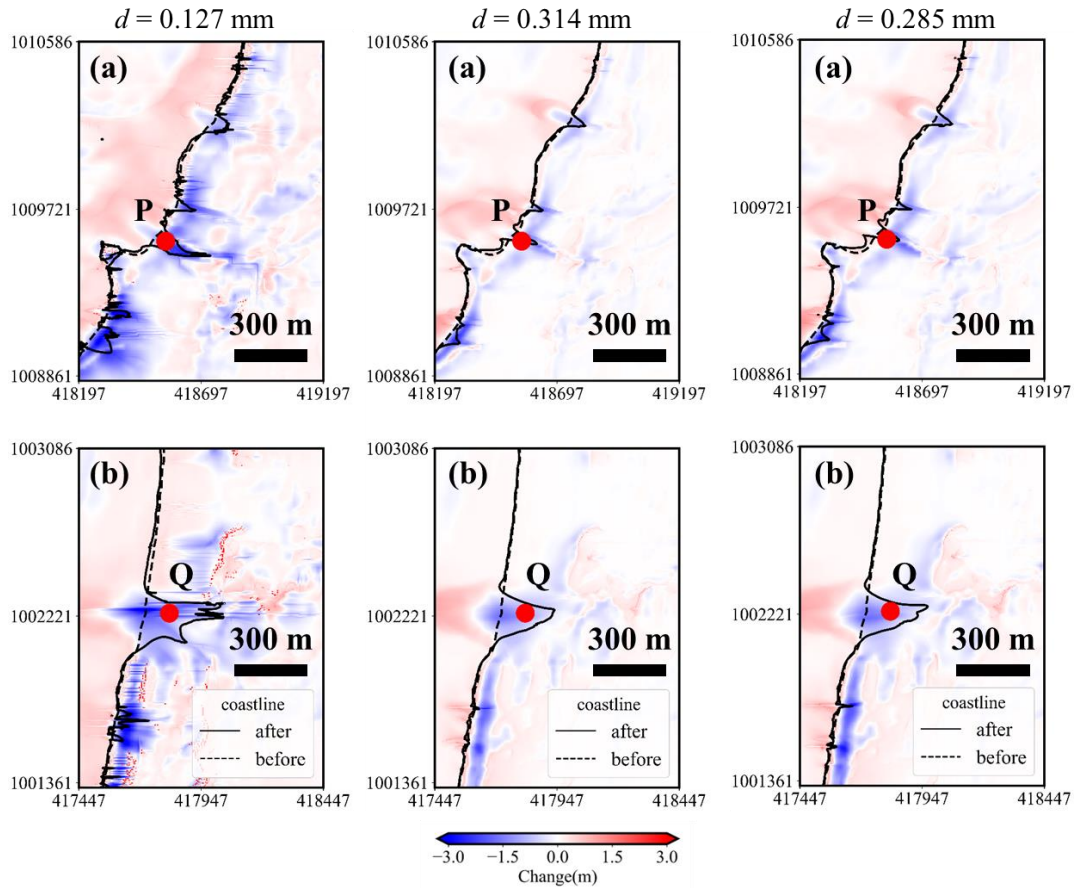
413 **Figure 8** Spatial distribution of measured and simulated thickness of tsunami deposits. The black dotted  
 414 lines indicate that the calculated values are underestimated at distances greater than 2 km.

415

416 conducted tsunami sediment transport simulation on the Sendai Plain and discussed the transportation  
 417 possibility of finer grained sandy and muddy sediment. Muddy sediments were also found in the Sendai  
 418 Plain at a distance of 2 km or more from the 2011 tsunami. Sugawara et al. (2014a)'s STM-based  
 419 tsunami sediment transport simulation could not be reproduced for Phra Thong Island, also due sandy  
 420 sediment and a single grain size model limitations. Therefore, it is possible that muddy or very fine-  
 421 grained sediment was deposited at the three sites but were underestimated in the simulations using the  
 422 current model.

423 Based on all above-mentioned reasons, it is more practical to evaluate the simulation results by the  
 424 overall trend of the tsunami deposit rather than comparing the thickness point by point. In Figure 7,  
 425 the line of "Cumulative volume" show the cumulative deposition expressed at each point by the  
 426 sediment thickness multiplied by the area of the computational grid. In general, the tsunami deposits  
 427 are greatly affected by local micro-topography (Sugawara et al., 2014a; Jaffe et al., 2016), and it is  
 428 difficult to fit the modelled layer thickness with the observed layer thickness using DEM averaged in a  
 429 computational grid. Therefore, we introduce the concept of cumulative sedimentation, and evaluated  
 430 the scale of the amount of sediment movement generated. Although the modelled layer thickness  
 431 typically overestimates the observed layer thickness by +7%, such low variation suggests a relatively  
 432 successful reproduction of the observed dataset (Figure 7). The modelled overestimation is likely due  
 433 to the assumption that the entire exposed land area would act as a movable bed. In reality, this is an  
 434 oversimplification of the true ground surface, which contains vegetation that binds and traps the soil





435

436

437

438

439

Figure 9 Topographic change and shoreline position caused by the tsunami for each grain size

Table 3 volume of erosion and deposition in regions (a) and (b) for each grain size (Percentage shows the ratio to reference)

	$d$ (mm)	Erosion (m <sup>3</sup> )		Deposition (m <sup>3</sup> )	
		Region (a)	Region (b)	Region (a)	Region (b)
Reference	0.127	352,333	314,189	259,379	254,417
Onshore	0.285	143,793 (41%)	155,225 (49%)	161,810 (62%)	149,470 (59%)
Offshore	0.314	117,491 (33%)	128,289 (41%)	137,749 (53%)	128,801 (51%)

440

441

442

443

444

445

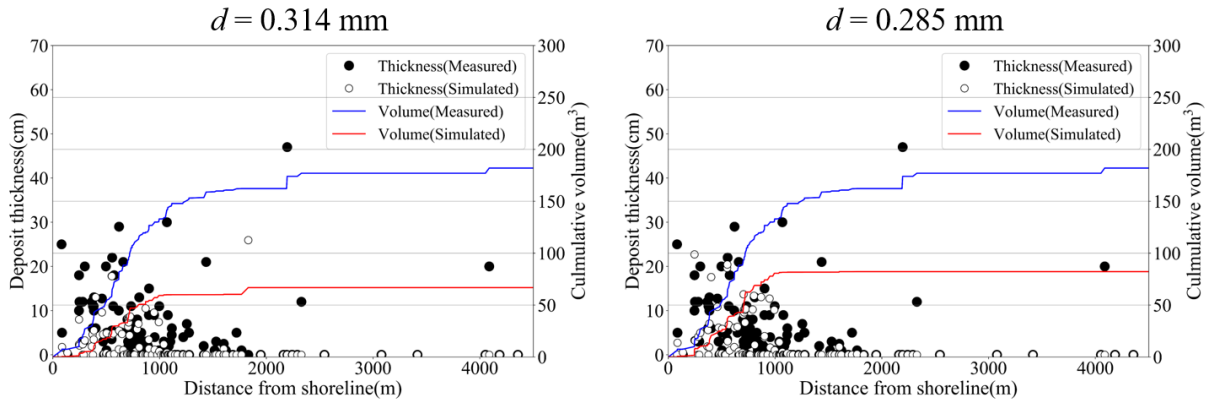
446

447

448

449

and wet regions (i.e. in swales) that would have higher degrees of sediment cohesion, reducing the area that would be eroded. In addition, the model also reproduces the inland thinning of the 2004 IOT deposit. **Based on these results, comparison of the sediment layer thickness of the 2004 tsunami shows that the scale and the overall sediment transport trend are comparable, and therefore, the results are sufficiently reproducible with confidence to evaluate the actual sediment transport.**



450

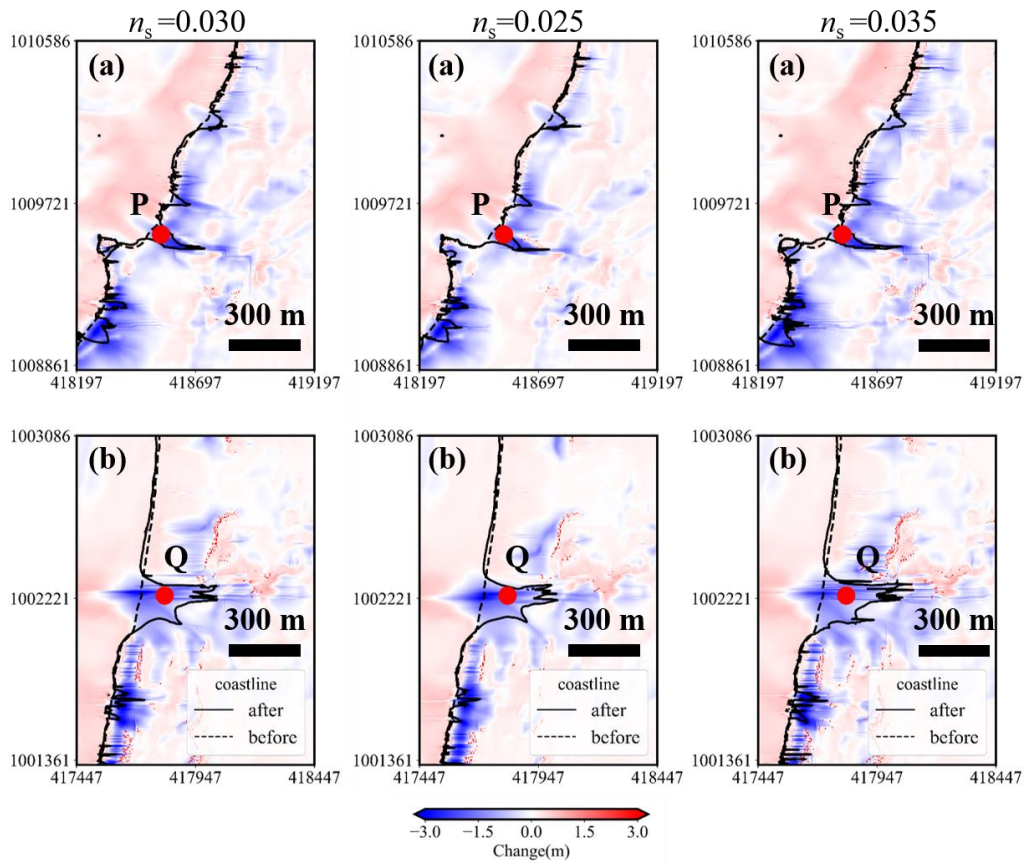
451 Figure 10 Comparison of field measured and simulated tsunami deposit thickness for each grain size.

452

### 453 3.1.4. Sensitivity analysis for grain size and roughness

454 Figure 9 shows the topographical changes and the thickness of the sediment layers used in this  
 455 calculation for each grain size, and Table 3 shows the volume of erosion and deposition in regions (a)  
 456 and (b). These figures show that smaller the particle size is, the greater the topographic change. This  
 457 can be understood by the smaller the particle size, the larger the Shields number in Eq. (10), which  
 458 indicates the ease of sediment transport, and the greater the amount of bed load in Eq. (8). However,  
 459 Figure 9 suggests that the qualitative characteristics of sediment transport are the same in the three  
 460 cases, due to the local erosion position of the beach in region (a) and (b) did not change for any particle  
 461 size. And then, comparing the tsunami sediment thickness in Figure 10 the errors of the cumulative  
 462 volume of  $d = 0.314$  mm and  $d = 0.285$  mm are -63% and -55%. Therefore, the grain size of  $d = 0.127$   
 463 mm is considered to show the better reproducibility.

464 Figure 11 shows the topographical changes and thickness of sediment layer in this calculation for each  
 465 bottom roughness coefficient, and Table 4 shows the volume of erosion and deposition in regions (a) and (b).  
 466 These figures show that larger the value of roughness coefficient  $n_s$  is, the greater the topographic change.  
 467 This can be understood by larger the roughness, the larger the Shields number in Eq. (10) because the friction  
 468 velocity is proportionate to  $n_s$ . Therefore, an increase in the roughness coefficient indicates the ease of  
 469 sediment transport, and the greater the amount of bed load in Eq. (8). However, Figure 11 suggests that the  
 470 qualitative characteristics of sediment transport are the same in the three cases, due to the local erosion  
 471 position of the beach in region (a) and (b) did not change for any bottom conditions. And then, comparing  
 472 the tsunami sediment thickness in Figure 12, the errors of the cumulative volume of  $n_s = 0.025$  s/m<sup>1/3</sup> and  
 473  $n_s = 0.035$  s/m<sup>1/3</sup> are -8% and 13%. Therefore, the roughness coefficient of  $n_s = 0.030$  s/m<sup>1/3</sup> is considered  
 474 to show the better reproducibility.



475

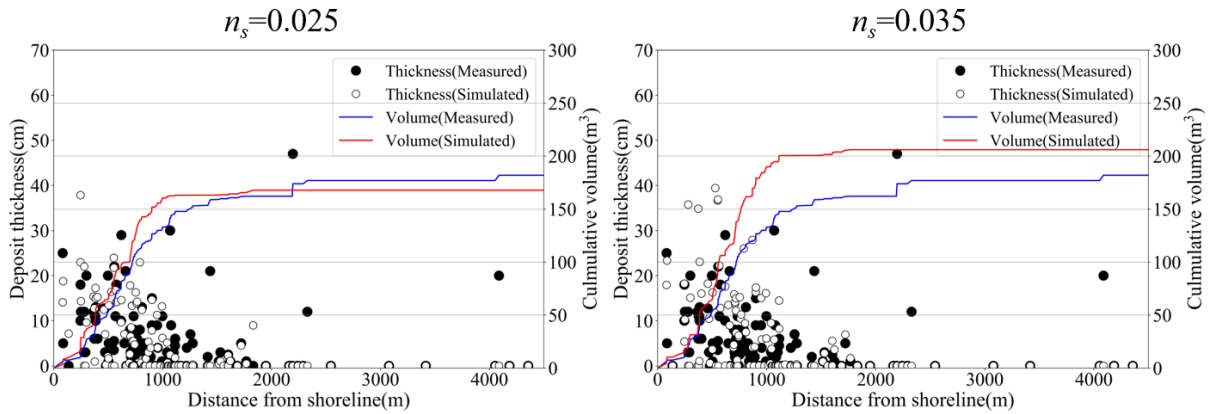
476 Figure 11 Topographic change and shoreline position caused by the tsunami for each **roughness**  
 477 **coefficient**

478

479 Table 4 volume of erosion and deposition in regions (a) and (b) for each roughness coefficient  
 480 (Percentage shows the ratio to reference)

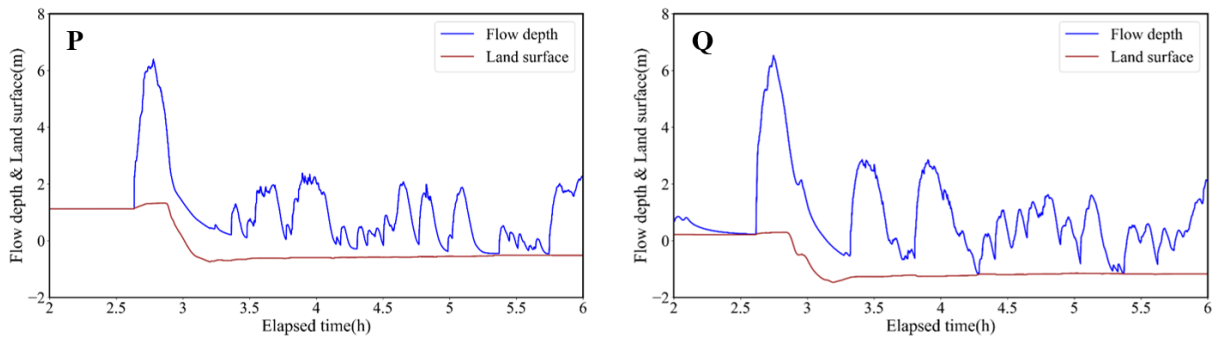
	$n_s$ ( $s/m^{1/3}$ )	Erosion ( $m^3$ )		Deposition ( $m^3$ )	
		Region (a)	Region (b)	Region (a)	Region (b)
Reference	0.030	352,333	314,189	259,379	254,417
Low	0.025	293,032 (83%)	285,659 (91%)	249,242 (96%)	230,905 (91%)
High	0.035	410,323 (116%)	352,284 (112%)	272,394 (105%)	262,522 (103%)

481



482  
483 Figure 12 Comparison of field measured and simulated tsunami deposit thickness for each roughness  
484 coefficient.

485



486  
487 Figure 13 Chronological change of flow depth and land surface at point P and Q in region (a) and (b)  
488 (blue line shows the flow depth and red line shows the land surface)

489

### 490 3.2. Sediment transport process

491 Although the model reproduces the zones of sediment erosion and deposition well, the sediment  
492 transport processes during the tsunami event are further examined in regions (a) and (b) in Figure 5.  
493 The modelled time series of the changes of water height and elevation at point P in region (a) and point  
494 Q in region (b) are shown in Figure 13. The modelling results show that the first wave arrived 2 hours 40  
495 minutes after the earthquake, and backwash was generated 10 minutes later (Figure 13). In addition, the  
496 ground surface elevation increased by about 30 cm through sediment deposition during the first  
497 inflowing wave and more than 1.5 m was eroded during the backwash transporting sediment towards  
498 the ocean, so beach loss in both regions is considered to be a result of erosion during the backwash (red  
499 line in Figure 13).

500 In addition, no major topographic changes occurred on the beaches in both areas after the second  
501 wave backwashed, most of the sediment movement on the eroded beaches is considered to have been  
502 completed by the second wave drawback. In other words, the sediment transport processes during this  
503 period are the most important to examine the shoreline changes that occurred during the tsunami and  
504 set up the primary conditions for beach recovery post-tsunami. As such, there are two narrow time  
505 periods that highlight the key factors that for establishing the initial conditions of the recovery process.

506 First, why was not the beach eroded by the inflowing waves? Second, how did the sediment flowing  
507 seaward in the first wave move?

508 Based on the waveform (which assumes a flat surface), a shore-normal cross section calculation was  
509 carried out along the transect in Figure 2. The transect covers the region (b) from 1000 m offshore across  
510 the shoreline and 1000 m inland. Beyond these distances the planar effect was considered to be  
511 negligible. Figure 14 shows the changes in ground level, water level, suspended sediment concentration  
512 and saturation of suspended sediment concentration on the transect at each unit of time as waves washed  
513 in and out.

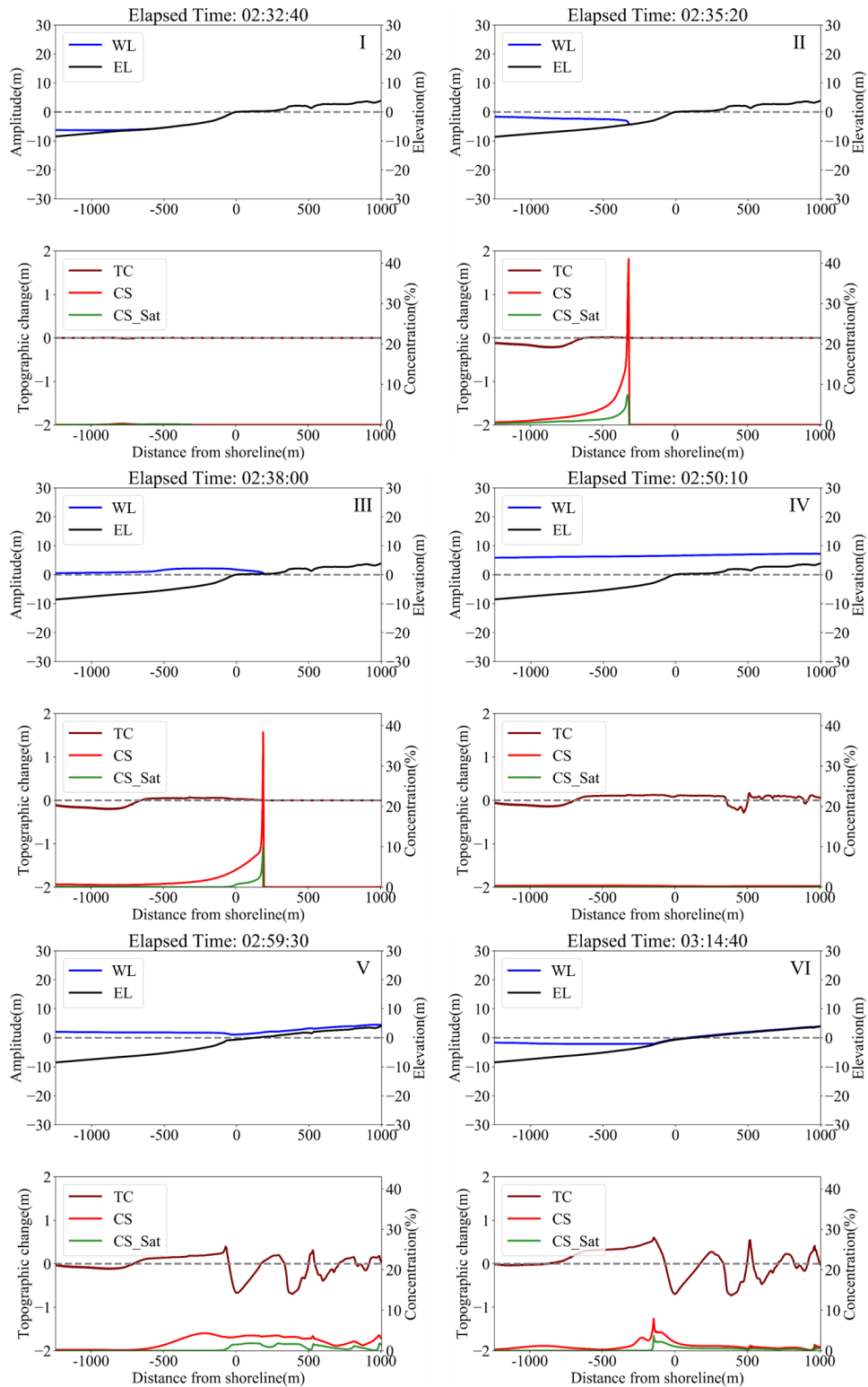
514

### 515 3.2.1 Why was not the beach eroded by the pushing wave?

516 As shown in Figure 14, prior to the first wave, the ocean receded to below approximately 8 m below  
517 mean sea level. As inflow of the first wave began, sediment was eroded from the sea floor at ca. 5-10m  
518 below mean sea level. This nearshore erosion increased the suspended sediment concentration as the  
519 first wave propagated onshore. At the shoreline, the suspended sediment concentration saturated and  
520 sedimentation could begin at the shoreline. In other words, it is estimated that sediment eroded the  
521 nearshore ( $5\text{ m} < \text{depth} < 10\text{ m}$ ) environment during the first inflowing wave, and much of this sediment  
522 was transported shoreline and inland.

523 It should be noted that, there will be no increase in suspended sediment when the suspended sediment  
524 is saturated in the model and is the likely reason that the beach was not eroded by the inflowing first  
525 wave. Although there is a possibility that the beach was actually eroded, the numerical results suggest  
526 that the erosion in shallow coastal waters (deeper than 5 m but shallower than 10 m) resulted in a very  
527 high concentration of suspended sediment when the inflowing first wave entered -5 m to the beach  
528 section of the coast and sediment ceased to be entrained. Pham et al. (2018) found that the source of the  
529 2004 IOT deposits on Phra Thong Island was from the nearshore (depth < 15m). This means that large  
530 scale erosion in shallow water has occurred and a large amount of sediment has been transported inland  
531 which agrees with the simulation results. Therefore, it is highly likely that the sediment concentration  
532 was very high when it reached the beach during the 1<sup>st</sup> inflowing wave. Takahashi (2012) showed that  
533 when the suspended sediment is in a high concentration state, turbulence is suppressed and the ability  
534 to retain suspended sediment may decrease. Therefore, it is highly probable that the same phenomenon  
535 occurred on Phra Thong Island and the beach erosion during the inflowing wave was suppressed.

536



537

538

539

540

541

542

543

Figure 14 Change in water level (WL), land surface (EL), topographic change (TC), suspended sediment concentration (CS), and saturation suspended sediment concentration (CS\_Sat) by section calculation along the survey line in region (b). (I) before the 1<sup>st</sup> inflowing wave, (II) Advance of 1<sup>st</sup> leading wave in shallow water, (III) Start of 1<sup>st</sup> leading wave run-up, (IV) Maximum of 1<sup>st</sup> leading wave , (V) Advance of 2<sup>nd</sup> backwash, (VI) Maximum of 2<sup>nd</sup> backwash

544 **3.2.2 *How did the sediment flowing seaward in the first wave move?***

545 In Figure 14, at the initiation of backwash, the suspended sediment concentration is low. As backwash  
546 flows towards the ocean, the velocity increases, which increases erosion and causes the suspended  
547 sediment concentration to increase. This finding is consistent with the changes recorded in Figure 13.  
548 Beach erosion due to backwash has also been confirmed in for the 2004 IOT in Sri Lanka and the 2011  
549 Tsunami along the Sendai Plain and at Rikuzentakata. (e.g. Tanaka et al., 2007, Tanaka et al. 2011,  
550 Yamashita et al. 2015, 2016). On the Sendai Plain, the estuary section of the old river tends to increase  
551 the return flow due to the tsunami (Tanaka et al., 2007, Tanaka et al. 2011). Therefore, there is a  
552 possibility that the region (a) and (b) (Fig. 2, 5 and 6) where local beach erosion of the backwash  
553 occurred on Phra Thong Island are the old river part.

554 Conversely, the entire beach was eroded by the return flow in Rikuzentakata (Yamashita et al., 2015,  
555 2016), but no erosion was observed along the entire beach on Phra Thong Island and the Sendai Plain.  
556 Yamashita et al. (2015, 2016) suggested that the difference between Rikuzentakata and the Sendai Plain  
557 may be related to the horizontal distance of the plains. On the Sendai Plain, the inland topographic  
558 gradient is small, the inundation distance is long and the inland inundation depth tends to be small.  
559 Therefore, the potential energy that the inundation depth changes to kinetic energy during the backwash  
560 (return flow) becomes relatively small. The Sendai Plain and Phra Thong Island are flooded plains over  
561 2 km inland and have similar topographical features.

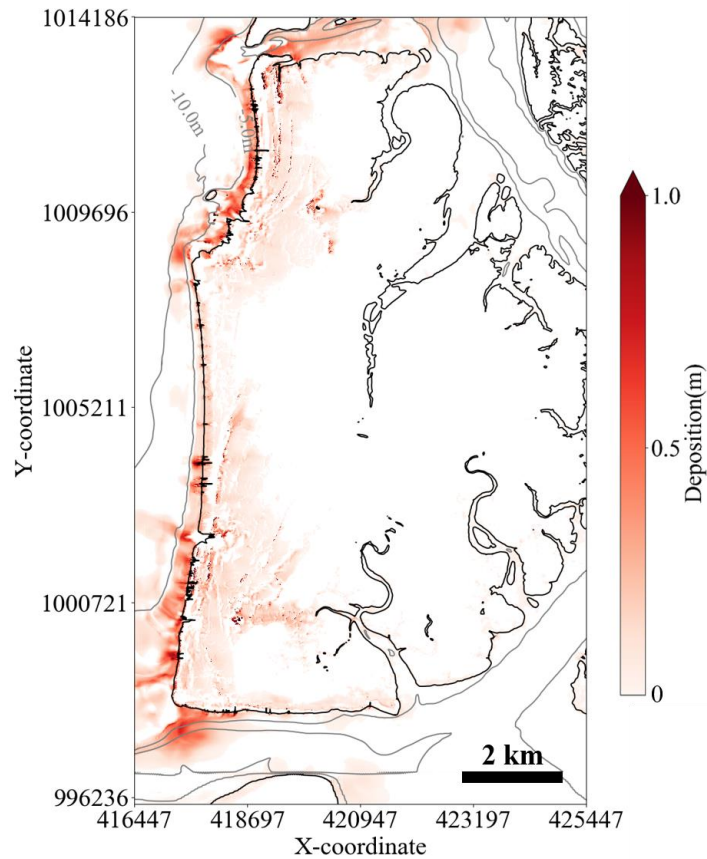
562 From the above reasons, the local beach erosion due to the return flow on Phra Thong Island occurred  
563 at the mouths of tidal channels and within tidal channels and that minimal erosion occurred across the  
564 wider beach ridge strand plain. As backwash of the first wave ended, the water still contained a high  
565 suspended sediment concentration and this was deposited in the nearshore environment at less than 5  
566 m water depth (Figure 15). After that, no significant topographic change was found. Thus, this  
567 modelling shows that most of the sediment that eroded from the onshore area was deposited in the  
568 shallow nearshore zone.

569  
570

571 **4. Discussion**

572 **4.1. *Sediment transport process and beach erosion***

573 Regions (a) and (b) were selected for detailed investigation of the simulation results and discussed.  
574 On Phra Thong Island, the 2004 IOT wave was large enough to expose the nearshore sediments and  
575 entrained most of its sediments from the shallow offshore region (below 5m). The wave ran up the  
576 exposed nearshore area while retaining sediment from the shallow offshore region. The sediment  
577 concentration gradually increases as the wave runs up the relatively long distance of the exposed  
578 nearshore zone, and became sediment-saturated as the wave reached the shoreline, making it difficult  
579 for new sediment to be eroded further. This explains why there was little erosion of the beach during  
580 the inflowing wave, and may be a characteristic sediment transport properties of shallow beaches like  
581 those on Phra Thong Island. The numerical simulation results suggest that there is little transportation



582  
 583 Figure 15 Sediment distribution derived from the simulation (showing depth contours at 5 m intervals  
 584 in the sea area)

585  
 586 of sediments from beach by the first inflowing wave and that inland tsunami deposits originated from  
 587 the nearshore environment. This finding validates Sawai et al. (2009)'s observation that the 2004 IOT  
 588 entrained diatoms from shallow offshore waters at Phra Thong Island, and Pham et al. (2018)'s  
 589 observation that sediment grain sizes and mineralogy were most similar to those of nearshore sediments.  
 590 Figure 15 shows the results of the calculated sediment deposition both onshore and offshore Phra Thong  
 591 Island. From the modelling results, most of the eroded sediment was deposited in shallow nearshore  
 592 environments in water less than approximately 5 m deep.

593 The simulations show that the eroded sediments were deposited in the nearshore zone during  
 594 backwash (Fig. 15), which primed the coastal zone for rapid coastal recovery. The removal of sediment  
 595 from the onshore coastal zone also generated accommodation space that may have contributed to the  
 596 coastal recovery process. Future studies can build on these findings to determine the extent of sediment  
 597 transport and deposition, and identify the processes of coastal recovery on Phra Thong Island.

598 Geomorphologically, the Sendai Plain, which was inundated by the March 11, 2011 Great East Japan  
 599 tsunami, is similar to the beach ridge plain on Phra Thong Island (Tanaka et al., 2011), but most of the  
 600 tsunami sediment deposited onshore came from terrestrial sources (Goto et al., 2012; Szczucin'ski et  
 601 al., 2012; Takashimizu et al., 2012; Sugawara et al., 2014b). However, the Great East Japan tsunami  
 602 differed from the 2004 IOT as the Japanese event had a much smaller receding wave (Nationwide Ocean



603 **Wave information network for Ports and HARbourS, NOWPHAS**). As such the Japanese tsunami may  
604 not have achieved sediment saturation as the wave approached the shoreline, thereby containing a lower  
605 sediment concentration and allowing large volumes of sediment to be entrained from the beach for  
606 subsequent formation of inland deposits. The different sources of deposited sediment in the two areas  
607 reflects contrasting sediment transport mechanisms on shallow beaches, and may be useful for  
608 identifying paleotsunami from coastal recovery and geological records.

609

#### 610 **4.2. Limits of calculation results**

611 This study analyzed tsunami sediment transport on Phra Thong Island using numerical calculations  
612 and assumed that the island was unvegetated and lacked topography. However, the western half of the  
613 island has an undulating surface caused by the beach ridge and swale system, and is extensively  
614 vegetated with trees and dense grasses on the ridges and thick grasses within the swales. The eastern  
615 half of the island has wide tidal channels and an extensive fringing mangrove system. Both topography  
616 and differing vegetation types add complexity to the inundation and backflow sediment transport  
617 models not captured here. In future, it is necessary to consider the influence of **vegetation** on tsunami  
618 sediment transport.

619 Another potential limitation of the model is the selection of a single (median) grain size for the  
620 sediments. As shown in previous studies (e.g. Sugawara et al., 2014a, b), the assumption of transport of  
621 single grain sized sediment differs from actual situations because of the distribution of grain sizes  
622 mobilised and deposited by tsunami. Therefore, it is important to set representative grain sizes and fully  
623 study how grain size affects tsunami sediment transport. Future modelling may consider simulating the  
624 suite of grain sizes individually or simulating a population of grain sizes that are identified in the modern  
625 environment and in preserved tsunami deposits.

626 Furthermore, although the calculation was performed considering the entire area a movable bed, the  
627 existence of fixed beds, such as rocky areas, should be considered. We consider this a minor component  
628 of this research as the rocky headlands that serve as fixed beds are relatively small in area and would  
629 contribute little to the overall simulations in our models.

630 Sugawara et al. (2014b) considers the simulation result of sediment layer thickness using the tsunami  
631 sediment transport calculation to be affected by grain size, bottom conditions and topographic data.  
632 Their study showed that the layer thickness increases as grain size becomes finer and the layer thickness  
633 distribution tendency was unchanged regardless of grain size. Similar results were obtained in this study.

634

635

#### 636 **5. Conclusion**

637 Because of insufficient knowledge about the topographic recovery process after a tsunami, this study  
638 used sediment transport modelling to identify the erosional and depositional processes affecting the  
639 coastal zone at Phra Thong Island, Thailand during the 2004 Indian Ocean Tsunami.

640 First, it was confirmed by comparing simulated results of the shoreline and sediment layer thickness

641 that the location of beach runoff identified on Phra Thong Island was reproducible and consistent with  
642 sediment transport results (Figs. 6 and 7). Based on the sediment transport results we conclude that the  
643 processes of sediment erosion and deposition on Phra Thong Island are characterized by the following  
644 sequence:

- 645 • erosion caused by the inflowing waves occurred at a relatively shallow location in the offshore  
646 area and the transported sediment was deposited near the shoreline;
- 647 • the inflowing waves caused minimal erosion of the shoreline; and,
- 648 • erosion of the shoreline was largely caused by backwash resulting in onshore sediments  
649 deposited in the shallow nearshore zone.

650 **These erosional and depositional processes demonstrate the locations of sediment removal and**  
651 **subsequent deposition during the different phases of the first tsunami wave on Phra Thong Island which**  
652 **will serve as an important baseline of sediment sources for further study of the recovery process.** The  
653 simulations also show that the zones of erosion and deposition across the island and offshore coastal  
654 zone are non-uniform. In particular, the zones of erosion and deposition highlighted in the simulations  
655 establish the environmental conditions that existed in the transitional phase between catastrophic  
656 tsunami and normal coastal processes that facilitated coastal recovery.

657

658

## 659 **6. Acknowledgements**

660 We would like to express our gratitude for the support from Dr. Panon Latcharote of the Faculty of  
661 Science and Technology of Thammasat University, Prof. Supot Teachavorasinskun, Dean of Faculty of  
662 Engineering, Chulalongkorn University, Dr. Pitcha Jongvivatsakul, Department of Civil Engineering  
663 Chulalongkorn University; and data from the Royal Thai Navy. RM, AS, KY, FI was support by JSPS  
664 Grant-in-Aid for Scientific Research (A) No. 17H01631 (FY2017 - FY2021). AS and NL was support  
665 by JSPS Bilateral program for joint research with National Research Council of Thailand (NRCT)  
666 (FY2017 - FY2018). CG was supported by NUS grant (R-109-000-223-133). NL was supported by  
667 Ratchadapisek Sompoch Endowment Fund (2019), Chulalongkorn University (762003-CC). This work  
668 is a contribution to IGCP Project 639, ‘Sea-level Change from Minutes to Millennia’.

669

## 670 **References**

- 671 1) Abe, T., Goto, K., and Sugawara, D.: Relationship between the maximum extent of tsunami sand  
672 and the inundation limit of the 2011 Tohoku–oki tsunami on the Sendai Plain, Japan, *Sedimentary*  
673 *Geology*, 282, 142–150, 2012.
- 674 2) Aida, I.: Reliability of a tsunami source model derived from fault parameters, *J. Phys. Earth*, 26,  
675 57–73, 1978.
- 676 3) Ali, P. Y., and Narayana, A. C.: Short-term morphological and shoreline changes at Trinkat Island,  
677 Andaman and Nicobar, India, after the 2004 tsunami. *Marine Geodesy*, 38(1), 26-39, 2015.
- 678 4) Arimitsu, T., Kawasaki, K., and Nimura, M.: Numerical simulation of sediment transport and

- 679 bottom topography change due to tsunami with large scale eddy, *Journal of JSCE, B2 (Coastal*  
680 *Engineering)*, 73, 2, 643–648, 2012.
- 681 5) Apotsos, A., Buckley, M., Gelfenbaum, G., Jaffe, B., and Vatvani, D.: Nearshore tsunami  
682 inundation model validation: toward sediment transport applications. *Pure and Applied*  
683 *Geophysics*, 168, 2097-2119, 2011a.
- 684 6) Apotsos, A., Gelfenbaum, G., and Jaffe, B.: Process-based modeling of tsunami inundation  
685 and sediment transport, *Journal of Geophysical Research*, 116, F01006, 2011b.
- 686 7) Apotsos, A., Gelfenbaum, G., Jaffe, B., Watt, S., Peck, B., Buckley, M., and Stevens, A.: Tsunami  
687 inundation and sediment transport in a sediment-limited embayment on American Samoa: *Earth-*  
688 *Science Reviews*, 107, 1-11, 2011c.
- 689 8) Bagnold, R. A.: An approach to the sediment transport problem from general physics. US  
690 government printing office, 1966.
- 691 9) Brill, D., Klasen, N., Jankaew, K., Brückner, H., Kelletat, D., Scheffers, A., and Scheffers, S.: Local  
692 inundation distances and regional tsunami recurrence in the Indian Ocean inferred from  
693 liminescence dating of sandy deposits in Thailand, *Natural Hazards and Earth System Sciences*,  
694 12, 2177–2192, 2012a.
- 695 10) Brill, D., Klasen, Brückner, H., Jankaew, K., Scheffers, A., Kelletat, D., and Scheffers, S.: OSL  
696 dating of tsunami deposits from Phra Thong Island, Thailand, *Quaternary Geochronology*, 10, 224–  
697 229, 2012b.
- 698 11) Brill, D., Jankaew, K., Bruckner, H.: Holocene evolution of Phra Thong's beach-ridge plain  
699 (Thailand) — Chronology, processes and driving factors, *Geomorphology*, 245, 117–134, 2015.
- 700 12) ChaguéGoff, C., Andrew, A., Szczuciński, W., Goff, J., and Nishimura, Y.: Geochemical  
701 signatures up to the maximum inundation of the 2011 Tohoku–oki tsunami — Implications for the  
702 869 AD Jogan and other palaeotsunamis, *Sedimentary Geology*, 282, 65–77, 2012.
- 703 13) Choowong, M., Phantuwongraj, S., Charoentitirat, T., Chutakositkanon, V., Yumuang S., and  
704 Charusiri, P.: Beach recovery after 2004 Indian Ocean tsunami from Phang-nga, Thailand,  
705 *Geomorphology*, 104, 134–142, 2009.
- 706 14) Fagherazzi, S. and Du, X.: Tsunamigenic incisions produced by the December 2004 earthquake  
707 along the coasts of Thailand, Indonesia and Sri Lanka, *Geomorphology*, 99, 120–129, 2008.
- 708 15) Feldens, P., Schwarzer, K., Szczuciński, W., Stattegger, K., Sakuna, D. and Sompongchaiyikul, P.  
709 Impact of 2004 tsunami on seafloor morphology and offshore sediments, Pakarang Cape, Thailand,  
710 *Polish Journal of Environmental Science* Vol. 18, No. 1, 63-68, 2009.
- 711 16) Fujino S., Naruse H., Matsumoto, D., Jarupongsakul T., Sphawajruksakul A., and Sakakura, N.:  
712 Stratigraphic evidence for pre–2004 tsunamis in southwestern Thailand, *Marine Geology*, 262, 25–  
713 28, 2009.
- 714 17) Fujino, S., Naruse, H., Matsumoto, D., Sakakura, N., Suphawajruksakul, A., and Jarupongsakul,  
715 T.: Detailed measurements of thickness and grain size of a widespread onshore tsunami deposit in  
716 Phang-nga Province, southwestern Thailand, *Island Arc*, 19, 389–398, 2010.

- 717 18) Gelfenbaum G., Vatvani D., Jaffe B., and Dekker F.: Tsunami inundation and sediment transport  
718 in vicinity of coastal mangrove forest, *Coastal Sediments*, 07, 1117-1128, 2007.
- 719 19) Goto, K., Takahashi, J., Oie, T., and Imamura, F.: Remarkable bathymetric change in the nearshore  
720 zone by the 2004 Indian Ocean tsunami: Kirinda Harbor, Sri Lanka, *Geomorphology*, 127, No.1-  
721 2, 107–116, 2011a.
- 722 20) Goto, K., ChaguéGoff, C., Fujino, S., Goff, J., Jaffe B., Nishimura, Y., Richmond, B., Sugawara,  
723 D., Szczuciński, W., Tappin, R. D., Witter, C. R., and Yuliant, E., New insights of tsunami hazard  
724 from the 2011 Tohoku–oki event, *Marine Geology*, 290, 46–50, 2011b.
- 725 21) Goto, K., Chague'Goff, C., Goff, J., and Jaffe, B.: The future of tsunami research following the  
726 2011 Tohoku–oki event, *Sedimen- tary Geology*, 282, 1–13, 2012.
- 727 22) Gouramanis, C., Switzer, A. D., Polivka, P. M., Bristow, C. S., Jankaew, K., Dat, P. T., Pile, J.,  
728 Rubin, C. M., Yingsin, L., Ildefonso, S. R., and Jol, H. M.: Ground penetrating radar examination  
729 of thin tsunami beds - A case study from Phra Thong Island, Thailand, *Sediment. Geol.*, 329, 149–  
730 165, 2015.
- 731 23) Gouramanis, C., Switzer, A. D., Jankaew, K., Bristow, C. S., Pham, D. T., and Ildefonso, S. R.:  
732 High-frequency coastal overwash deposits from PHRA thong Island, Thailand, *Sci. Rep.*, Vol.7,  
733 No. September 2016, 1–9, 2017.
- 734 24) Gusman, A. R., Tanioka, Y., and Takahashi, T.: Numerical experiment and a case study of sediment  
735 transport simulation of the 2004 Indian Ocean tsunami in Lhok Nga, Banda Aceh, Indonesia., *Earth*,  
736 *planets and space*, 64, 817-827, 2012.
- 737 25) Haraguchi, T., Takahashi, T., Hisamatsu, R., Morishita, Y., and Sasaki, I.: A Field Survey of  
738 Geomorphic Change on Kessenuma Bay caused by the 2010 Chilean Tsunami and the 2011  
739 Tohoku Tsunami, *Journal of JSCE*, B2 (Coastal Engineering), 68, 231–235, 2012.
- 740 26) Hawkes, A.D., Bird, M., Cowie, S., Grundy-Warr, C., Horton, B.P., Hwai, A.T.S., Law, L.,  
741 Macgregor, C., Nott, J., Ong, J.E., Rigg, J., Robinson, R., Tan-Mullins, M., Sa, T.T., Yasin, Z., Aik,  
742 L.W.: Sediments deposited by the 2004 Indian Ocean Tsunami along the Malaysia–Thailand  
743 Peninsula, *Marine Geology*, 242, 169–190, 2007.
- 744 27) Hirao, R., Tanaka, H., Umeda, M., Adityawan, M. B., Mano, A., and Udo, K.: Breaching of Sandy  
745 Coast and Spit Due To The 2011 Tsunami and Their Recovery, *Journal of JSCE*, B2(Coastal  
746 Engineering), 68, 581–585, 2012.
- 747 28) Imai, K., Sugawara, D., Takahashi, T., Iwama, S., and Tanaka, H.: Numerical study for sediment  
748 transport due to tsunami around the Kitakami River mouth, *Journal of JSCE*, B2(Coastal  
749 Engineering), 71, 247–252, 2015.
- 750 29) Imamura, F.: Review of tsunami simulation with a finite difference method, in: *Long-Wave Runup*  
751 *Models*, edited by: Yeh, H., Liu, P., and Synolakis, C. E., World Scientific Publishing Co.,  
752 Singapore, 25–42, 1996.
- 753 30) Iwagaki, Y.: Hydrodynamical study on critical tractive force, *Trans. JSCE*, 41(41), 1–21, 1956.
- 754 31) Jaffe, B., Goto, K., Sugawara, D., Gelfenbaum, G., and La Selle, S.: Uncertainty in tsunami

- 755 sediment transport modeling. *Journal of Disaster Research*, 11(4), 647-661, 2016.
- 756 32) Jankaew, K., Atwater, B. F., Sawai, Y., Choowong, M., Charoentitirat, T., Martin, M. E., and  
757 Prendergast, A.: Medieval forewarning of the 2004 Indian Ocean tsunami in Thailand, *Nature*,  
758 455(7217), 1228–1231, 2008.
- 759 33) Koiwa, N., Takahashi, M., Sugisawa, S., Ito, A., Aki Matsumoto, H., Tanavud, C., and Goto, K.:  
760 Barrier spit recovery following the 2004 Indian Ocean tsunami at Pakarang Cape, southwest  
761 Thailand, *Geomorphology*, 306, 314–324, 2018.
- 762 34) Land Development Department of Thailand (LDD) Maps and mapping information, Available at:  
763 [http://www.ddd.go.th/www/lek\\_web/web.jsp?id=19273](http://www.ddd.go.th/www/lek_web/web.jsp?id=19273) (Accessed date: 18 October 2017)
- 764 35) Li, L., Qiu, Q., and Huang, Z.: Numerical modeling of the morphological change in Lhok Nga,  
765 west Banda Aceh, during the 2004 Indian Ocean tsunami: understanding tsunami deposits using a  
766 forward modeling method, *Natural Hazards*, 64, 1549-1574, 2012.
- 767 36) Li, L., Huang, Z., and Qiu, Q.: Numerical simulation of erosion and deposition at the Thailand  
768 Khao Lak coast during the 2004 Indian Ocean tsunami, *Natural Hazards*, 74, 2251-2277, 2014.
- 769 37) Liew, S.C., Gupta, A., Wong, P.P., Kwoh, L.K.: Recovery from a large tsunami mapped over time:  
770 The Aceh coast, Sumatra, *Geomorphology*, 114, 520–529, 2010.
- 771 38) Morishita, Y., and Takahashi, T.: Accuracy improvement of movable bed model for tsunamis by  
772 applying for Kesennuma bay when the 2011 Tohoku tsunami arrived, *Journal of JSCE, B2(Coastal*  
773 *Engineering)*, 70, 491–495, 2014.
- 774 39) Rubey, W. W.: Settling velocity of gravel, sand, and silt particles. *American Journal of Science*,  
775 148, 325-338, 1933.
- 776 40) Saegusa, S., Tanaka, H., and Mitobe, Y.: Recovery processes of bathymetry of Sendai Bay after the  
777 2011 tsunami, *Journal of JSCE, B2(Coastal Engineering)*, 73, 817–822, 2017.
- 778 41) Okada, Y.: Surface deformation due to shear and tensile faults in a half-space, *Bulletin of the*  
779 *Seismological Society of America*, 75(4), 1135–1154, 1985.
- 780 42) Pari, Y., Ramana Murthy, M. V., Jaya Kumar, S., Subramanian, B. R., and Ramachandran, S.:  
781 Morphological changes at Vellar estuary, India — Impact of the December 2004 tsunami, *Journal*  
782 *of Environmental Management*, 89, 45–57, 2008.
- 783 43) Paris, R., Lavigne, F., Wassmer, P., Sartohadi, J.: Coastal sedimentation associated with the  
784 December 26, 2004 tsunami in Lhok Nga, west Banda Aceh (Sumatra, Indonesia), *Marine Geology*,  
785 238, 93–106, 2007.
- 786 44) Pham, T. D., Gouramanis, C., Switzer, M. A., Rubin, M. C., Jones, G. B., Jankaew, K., and Carr,  
787 F. P.: Elemental and mineralogical analysis of marine and coastal sediments from Phra Thong  
788 Island, Thailand: Insights into the provenance of coastal hazard deposits, *Marine Geology*, 385,  
789 274–292, 2018.
- 790 45) Prendergast, L. A., Cupper L. M., Jankaew, K., and Sawai, Y.: Indian Ocean tsunami recurrence  
791 from optical dating of tsunami sand sheets in Thailand, *Marine Geology*, 295–298, No.15, 20–27,  
792 2012.

- 793 46) Sawai, Y., Jankaew K., Martin, E. M., Prendergast, A., Choowong, M., and Charoentitirat, T.:  
794 Diatom assembles in tsunami deposits associated with th 2004 Indian Ocean tsunami at Phra Thong  
795 Island, Thailand, *Marine Micropaleontology*, 73, 70–79, 2009.
- 796 47) Sugawara, D., Goto, K., and Jaffe, B. E.: Numerical models of tsunami sediment transport –Current  
797 understanding and future directions, *Marine Geology*, 352, 295–320, 2014a.
- 798 48) Sugawara, D., Takahashi, T., and Imamura, F.: Sediment transport due to the 2011 Tohoku-oki  
799 tsunami at Sendai: Results from numerical modeling, *Mar. Geol.*, 358, 18–37, 2014b.
- 800 49) Suppasri, A., Koshimura, S., and Imamura, F.: Developing tsunami fragility curves based on the  
801 satellite remote sensing and the numerical modeling of the 2004 Indian Ocean tsunami in Thailand,  
802 *Nat. Hazards Earth Syst. Sci.*, 11(1), 173–189, 2011.
- 803 50) Suppasri, A., Latcharote, P., Bricker, J. D., Leelawat, N., Hayashi, A., Yamashita, K., Makinoshima,  
804 F., Roeber, V. and Imamura, F.: Improvement of tsunami countermeasures based on lessons from  
805 the 2011 great east japan earthquake and tsunami -Situation after five years-, *Coastal Engineering*  
806 *Journal*, 58 (4), 1640011, 2016.
- 807 51) Switzer, A.D., Srinivasalu, S., Thangadurai, N., Ram Mohan, V.: Bedding structures in Indian  
808 tsunami deposits that provide clues to the dynamics of tsunami inundation, *Geological Society,*  
809 *London, Special Publications*, 361, 61-77, 2012.
- 810 52) Szczuciński, W., Kokociński, M., Rzeszewski, M., Chahué–Goff, C., Cachão, M., Goto, K., and  
811 Sugawara, D.: Sediment sources and sedimentation processes of 2011 Tohoku–oki tsunami  
812 deposits on the Sendai Plain, Japan — Insights from diatoms, nannoliths and grain size distribution,  
813 *Sedimentary Geology*, 282, 40–56, 2012.
- 814 53) Takahashi, T., Shuto, N., Imamura, F., and Asai, D.: Modeling sediment transport due to tsunamis  
815 with exchange rate between bed load layer and suspended load layer, *Proceedings Of International*  
816 *Conference of Coastal Engineering*, 1508–1519, 2000.
- 817 54) Takahashi, J., Goto, K., Oie, T., Yanagisawa, H., and Imamura, F.: Inundation and topographic  
818 Change due to the 2004 Indian Ocean Tsunami at the Kirinda port, Sri Lanka, *Journal of JSCE,*  
819 *B2(Coastal Engineering)*, 55, 251–255, 2008.
- 820 55) Takahashi, T., Kurokawa, T., Fujita, M., and Shimada, H.: Hydraulic experiment on sediment  
821 transport due to tsunamis with various sand grain size, *Journal of JSCE, B2(Coastal Engineering),*  
822 *67, 231–235, 2011.*
- 823 56) Takahashi, T.: Numerical modeling if sediment transport due to tsunamis and its problem, *Journak*  
824 *of the Sedimentological Society of Japan*, 71, 2, 149-155, 2012.
- 825 57) Takashimizu, Y., Urabe, A., Suzuki, K., and Sato, Y.: Deposition by the 2011 Tohoku–oki tsunami  
826 on coastal lowland controlled by beach ridges near Sendai, Japan, *Sedimentary Geology*, 282, 124–  
827 141, 2012.
- 828 58) Tanaka, H., Ishino, K., Nawarathna, B., Nakagawa, H., and Yano, S.: Coastal and river mouth  
829 morphology change in Sri Lanka due to the 2004 Indian Ocean Tsunami. In *Coastal Sediments' 07*  
830 (pp. 842-855), 2007.

- 831 59) Tanaka, H., Mano, A., and Udo, K.: Beach Morphology Change Induced by The 2011 Great East  
832 Japan Earthquake Tsunami, *Journal of JSCE, B2(Coastal Engineering)*, 67(2), 571–575, 2011.
- 833 60) Udo, K., Tanaka, H., Mano, A., and Takeda, Y.: Beach Morphology Change of Southern Sendai  
834 Coast due to 2011 Tohoku Earthquake Tsunami, *Journal of JSCE, B2(Coastal Engineering)*, 69,  
835 391–395, 2013.
- 836 61) Udo, K., and Takeda, Y.: Comparison between characteristics of shoreline changes due to the 2004  
837 Indian Ocean tsunami and the 2011 Great East Japan tsunami, *Journal of JSCE, B3(Coastal*  
838 *Engineering)*, 72, 175–180, 2016.
- 839 62) Van Rijn, L. C.: Unified view of sediment transport by currents and waves. I: Initiation of motion,  
840 bed roughness, and bed-load transport. *Journal of Hydraulic engineering*, 133(6), 649-667, 2007.
- 841 63) Watanabe, A., Maruyama, Y., Shimizu, T., and Sakakiyama, T.: Numerical prediction model of  
842 three-dimensional beach transformation due to installed structures, *Journal of JSCE(Coastal*  
843 *Engineering)*, 31, 406–410, 1984.
- 844 64) Watanabe, M., Goto, K., Bricker, J. D., and Imamura, F.: Are inundation limit and maximum extent  
845 of sand useful for differentiating tsunamis and storms? An example from sediment transport  
846 simulations on the Sendai Plain, Japan. *Sedimentary geology*, 364, 204-216, 2018.
- 847 65) Xu, J.: Grain-size characteristics of suspended sediment in the Yellow River, China, *Catena*, 38,  
848 243-263, 1999a.
- 849 66) Xu, J.: Erosion caused by hyperconcentrated flow on the Loess Plateau of China, *Catena*, 36, 1-19,  
850 1999b.
- 851 67) Yamashita, K., Sugawara, D., Takahashi, T., Imamura, F., Saito, Y., Imato, Y., Kai, T., Uehara, H.,  
852 Kato, T., Nakata, K., Saka, R., and Nishikawa, A.: Numerical simulation of large-scale sediment  
853 transport due to the 2011 tohoku earthquake tsunami in Rikuzentakata city, *Journal of JSCE,*  
854 *B2(Coastal Engineering)*, 71, 499–504, 2015.
- 855 68) Yamashita, K., Sugawara, D., Takahashi, T., Imamura, F., Saito, Y., Imato, Y., and Saka, R.:  
856 Numerical simulations of large-scale sediment transport caused by the 2011 Tohoku Earthquake  
857 Tsunami in Hirota Bay, Southern Sanriku Coast. *Coastal Engineering Journal*, 58(04), 2016.
- 858 69) Yamashita, K., Shigihara, Y., Sugawara, D., Arikawa, T., Takahashi, T., and Imamura, F.: Effect of  
859 sediment transport on tsunami hazard and building damage –an integrated simulation of tsunami  
860 inundation, sediment transport and drifting vessels in Kesennuma city, Miyagi prefecture during  
861 the great east Japan –, *Journal of JSCE, B2(Coastal Engineering)*, 73, 355–360, 2017.
- 862 70) Yamashita, K., Sugawara, D., Arikawa, Y., Takahashi, T., and Imamura, F.: Improvement of  
863 tsunami-induced sediment transport model by considering saturated concentration in suspension  
864 with strong unsteady flows, *Journal of JSCE, B2(Coastal Engineering)*, 69, 325–330, 2018.
- 865 71) Yunus Ali, P., and Narayana, A. C.: Short-Term Morphological and Shoreline Changes at Trinkat  
866 Island, Andaman and Nicobar, India, After the 2004 Tsunami, *Marine Geodesy*, 38, 26–39, 2015.
- 867